Lattice dynamics and magnetic properties in selected functional iron compounds

Faculté des Sciences - Université de Liège

&

Jülich Centre for Neutron Science (JCNS-2)

and Peter Grünberg Institute (PGI-4)

- Forschungszentrum Jülich GmbH

Année académique 2014-2015

Dissertation présentée par
Marcus Herlitschke
en vue de l'obtention du grade de
Docteur en Sciences

Preface

Abstract

The presented thesis reports about to the investigation of four different materials with respect to their magnetic properties and their lattice dynamics.

The carbodiimide FeNCN, which was recently synthesized for the first time and can be considered as an non-oxidic analogue to FeO, is discussed in chapter 2. The NCN^{2-} group bridges two iron and exhibits a double negative charge, similar to the oxygen in FeO. This material exhibits an increased magnetic order temperature as compared to FeO. FeNCN was investigated with magnetometry, Mössbauer spectroscopy and nuclear inelastic scattering, revealing an unusual behaviour of the hyperfine parameters below the ordering temperature. This observation is discussed with respect to the crystal field and the *d*-orbital level population with temperature.

The investigation of the magnetocaloric material $Mn_{5-x}Fe_xSi_3$ is reported in chapter 3 with focus on the interaction of magnetism and lattice dynamics. Among the $Mn_{5-x}Fe_xSi_3$ compounds, $MnFe_4Si_3$ is the most interesting one due to the possible application as a room temperature refrigeration material. The investigation reveals that a direct measurement of the influence of the magnetocaloric effect on the density of iron phonon states is not possible, however, the elasticity was observed to be strongly influenced by this effect.

The studies on the spin orientation in nanospheres and a NANOPERM alloy are discussed in chapter 4 and chapter 5. Two approaches were followed in order to investigated the spin orientation, nuclear forward scattering and nuclear resonant small-angle X-ray scattering. In the first part, maghemite nanospheres are analysed with in-field nuclear forward scattering, revealing that the spins orient only partially along the direction of the applied magnetic field. A modeled magnetization calculated from the observed degree of spin orientation matches excellently the macroscopic magnetometry data and literature values. Though revealing the amount of oriented spins, nuclear forward scattering is not sensitive to their position in the nanoparticles. Thus, the nuclear forward scattering was combined with small-angle X-ray scattering, leading to small-angle patterns in dependence of the local spin orientation in the aforementioned samples.

Résumé

Ce travail concerne l'étude des propriétés magnétiques et dynamiques des quatre matériaux différents.

Le carbodiimide FeNCN synthétisé récemment pour la première fois et considéré comme un composé non oxydique analogue à FeO est discuté dans le chapitre 2. Le groupe NCN lié deux atomes de fer et présente une double charge négative semblable à celle de O dans l'oxyde de fer FeO. Par contre, ce matériau montre une important augmentation de la température d'ordre magnétique par rapport à FeO. Le composé FeNCN a été étudié par différentes techniques expérimentales: La magnétométrie, la spectroscopie Mössbauer et la diffusion inélastique nucléaire ce qui a révélé un comportement inhabituel des paramètres hyperfins en dessous de la température d'ordre magnétique. Ces observations sont discutées en termes de champs cristallin et de la population des orbitales *d* en fonction de la température.

L'étude des matériaux magnétocalorique $Mn_{5-x}Fe_xSi_3$ est rapportée dans le chapitre 3 avec un intérêt particulier pour les interactions magnétiques et les propriétés de dynamique du réseau. Parmi les composés $Mn_{5-x}Fe_xSi_3$, $MnFe_4Si_3$ présente les propriétés les plus intéressantes pour une utilisation à température ambiante comme un matériau de réfrigération. Notre étude révèle que l'effet magnétocalorique n'a aucune influence measurable sur la densité d'états de phonons. Cependant, l'élasticité est fortement influencée par la transition magnétique associée.

Les études de l'orientation de spin dans les nanosphères et l'alliage NANOPERM sont discutées dans les chapitres 4 et 5. Deux approches ont été suivies pour l'analyse de l'orientation de spin: la diffusion nucléaire résonante vers l'avant et la diffusion nucléaire résonante aux petits angles. Dans la première partie de cette étude, des nanosphères de maghémite sont analysées par diffusion nucléaire vers l'avant sous champs appliqué, qui indique que les spins sont seulement partiellement orientés le long du champ magnétique appliqué. Une aimantation modélisée calculée à partir du degré d'ordre observé, est en très bon accord avec les données de magnétométrie macroscopique et la littérature. Cependant, la diffusion nucléaire vers l'avant n'est pas sensible à la position des spins orientés à l'intérieur des nanoparticules. Ainsi, la diffusion nucléaire vers l'avant a été combinée avec la diffusion des rayons X aux petits angles, ce qui nous a permis d'obtenir la diffraction aux petits angles, en fonction de l'orientation locale des spins dans les nanoparticules et l'alliage susmentionnés.

Kurzzusammenfassung

Das vorliegende Manuskript beschreibt die Untersuchung von vier verschiedenen Materialien, hinsichtlich ihrer magnetischen Eigenschaften und ihrer Gitterdynamik.

Das Kapitel 2 beschäftigt sich mit dem Karbodiimide FeNCN, welches erst kürzlich zum ersten mal synthetisiert wurde und als Analogon zu FeO aufgefasst werden kann. Die NCN^{2-} Gruppe verbindet zwei Eisenatome und ist dabei zweifach negativ geladen, wie auch das Sauerstoffatom in FeO. Dieses Material weist jedoch, hinsichtlich seiner magnetischen Eigenschaften, einige markante Unterschiede zu FeO auf. FeNCN wurde mittels Magnetometrie, Mössbauer Spektroskopie und Nuklearer-Inelastischer-Streuung untersucht und es wurde ein ungewöhnliches Verhalten der hyperfeinen Parameter in diesem Material unterhalb der Ordnungstemperatur beobachtet. Diese Beobachtungen sind bezüglich der Temperaturabhängigkeit der *d*-Orbitalbesetzung diskutiert.

Im 3ten Kapitel wird die Untersuchung der magnetokalorische Verbindung $Mn_{5-x}Fe_xSi_3$ beschrieben. Der Hauptaspekt der Untersuchung ist die Interaktion zwischen Magnetismus und Gitterdynamik in diesem Material. Die Verbindung $MnFe_4Si_3$ ist von besonderem Interesse, da dieses Material seine magnetische Ordnungstemperatur bei $\sim 300\,\mathrm{K}$ hat und deshalb zum magnetischen Kühlen bei Raumtemperatur genutzt werden kann. Die Untersuchungen ergaben, dass der direkte Nachweis des magnetokalorischen Effektes mittels Nuklearer-Inelastischer-Streuung nicht möglich ist aber der magnetische Übergang einen großen Einfluss auf die Elastizität des Materials besitzt.

Die Kapitel 4 und 5 berichten über die Untersuchungen an der Spinorientierung in Maghemite-Nanospheren und einer Legierung aus der NANOPERM Gruppe. Die Ergebnisse sind in zwei Kapitel aufgeteilt, da sie über zwei unterschiedliche Herangehensweisen der Untersuchung handeln. Im ersten Teil wird die Nukleare-Vorwärts-Streuung im angelegten Magnetfeld genutzt, um den prozentualen Anteil an ausgerichteten Spins in den Nanospheren in Abhängigkeit vom angelegten Magnetfeld zu beobachten. Es wurde gezeigt, dass sich nur ein Teil der Spins im magnetischem Feld ausrichtet, woraus eine modellierte Magnetisierung berechnet wurde, die hervorragend mit der makroskopisch gemessenen Magnetisierung und Literaturwerten übereinstimmt. Da diese Methode nur den Grad der Spinorientierung wiedergibt, aber nicht die Position der Spins im Nanopartikel, wurde im zweiten Teil der Untersuchung die Nukleare-Vorwärts-Streuung mit der Kleinwinkel-Streuung ergänzt. Diese Methode führt zu Kleinwinkelstreuung in Abhängigkeit von der lokalen Spinorientierung in den erwähnten Proben.

Acknowledgements

During my thesis, a variety of people supported me and my work and I would like to thank them at this point.

The first person to thank is my supervisor Prof. Raphael Hermann for the opportunity to write this thesis, his avid interest in my work and his support. Especially the freedom in the choice of my scientific topic and the access to different projects and scientific issues allowed me to work on a manuscript representing my interest.

I want to thank also my co-advisor at the Université de Liège Prof. Rudi Cloots, as well as Prof. Bénédicte Vertruyen, Prof. Manuel Angst, and Prof. Alejandro Silhanek for being members of the thesis jury. Further, I acknowledge Prof. Jean-Marc Grenèche and Prof. Daniel Nižňanský to be so kind to act as external referees.

I acknowledge Prof. Thomas Brückel, as director of JCNS-2, for the possibility to work in an international environment and for the access to the large amount of in-house methods.

Dr. Benedikt Klobes, Dr. Ilya Sergeev, and Dr. Sabrina Disch are acknowledged for their support in measurements and the subsequent analysis. There was always an open door for me and their support was always very useful.

I would also like to thank the other members of Prof. Raphael Hermann's group, *i.e.*, Ronnie Simon, Dr. Abdelfattah Mahmoud, Atefeh Jafari, Dr. Vasily Potapkin, Mikheil Mebonia, and Pavel Alexeev, for their assistance in measurements and especially for the friendly and social time we had together. The same counts for all other members of JCNS-2/PGI-4, too. Thanks a lot. Special thanks go to Jörg Perßon, Frank Gossen and Berthold Schmitz, who always found a quick solution for urgent sample preparation and technical problems.

I acknowledge all co-authors for their contributions, the interesting discussions and the helpful assistance they offered me for our various investigations.

Portions of this research were carried out at the light source PETRA III at DESY, a member of the Helmholtz Association (HGF), and at the European Synchrotron Radiation Facility (ESRF), Grenoble. I am very thankful for the granted beam times and the support, which I received.

I particularly acknowledge the local contacts at the large-scale facilities ESRF and PETRA III, *i.e.*, Dr. Kai Schlage, Dr. Hans-Christian Wille, Dr. Dimitrios Bessas, Dr. Sascha Chumakov and Dr. Rudolf Rüffer, for the assistance in using the beam lines and the subsequent data analysis. This technical support is essential and can not be acknowledged often enough.

Last but not least, I have to thank my whole family for their support and especially for their patience.

Vita

Marcus Herlitschke was born on 11.04.1985 in Finsterwalde, Germany. After receiving the general qualification for university entrance from Janusz-Korczak Gymnasium in Finsterwalde, he studied physics at the Brandenburgische Technische Unversität Cottbus (BTU). He prepared his diploma thesis at the Fraunhofer Institute für Photonische Mikrosysteme (IPMS) in Dresden in cooperation with the BTU. In 2011, he started his doctoral research under supervision of Dr. R. Hermann at the Univerity de Liège and Forschungzentrum Jülich.

Publications during the thesis

(1) M. Herlitschke, A. L. Tchougréff, A. V. Soudackov, B. Klobes, L. Stork, R. Dronskowskic and R. P. Hermann: **Magnetism and Lattice Dynamics of FeNCN compared to FeO**, *New J. Chem.*, **38**, (2014), 4670
Front cover October 2014

(2) D. Vidick, M. Herlitschke, C. Poleunis, A. Delcorte, R. P. Hermann, M. Devillersa and S. Hermans: **Comparison of functionalized carbon nanofibers and multi-walled carbon nanotubes as supports for Fe-Co nanoparticles**, *J. Mater. Chem. A*, **1**, (2013), 2050-2063.
M. Herlitschke contributed the magnetometric measurements and the analysis.

(3) J. G. Mahy, L. Tasseroul, A. Zubiaur, J. Geens, M. Brisbois, M. Herlitschke, R. Hermann, B. Heinrichs, S. D. Lambert: **Highly dispersed iron xerogel catalysts for p-nitrophenol degradation by photo-Fenton effects**, *Microporous and Mesoporous Materials*, **197**, (2014), 164-173
M. Herlitschke contributed the magnetometric measurements and the analysis.

Best Poster Awards

(1) International Conference on the Applications of the Mössbauer Effect - ICAME 2013, Opatija: **Mössbauer Spectroscopic Investigation of the Unconventional Hyperfine Field Behavior in FeNCN**.

(2) Groupe Francophone de Spectrométrie Mössbauer - GFSM 2014, Montpellier: **The spin structure in γ-Fe2O3 nanoparticles - investigated in field with polarized nuclear resonant scattering**.

Contents

Chapter 1

1 Introduction

This chapter introduces the scope of the thesis and gives an overview of the physical effects discussed in the experimental part. The presentation should not be considered as a complete description of all phenomena related to the given topics, but rather as a first insight into these phenomena in order to provide the necessary information and to foster understanding. Furthermore, selected models and formulas, which are important for the analysis of the experimental data, are also given.

1.1 General Introduction

For emerging technologies, the demand of efficiency and energy saving becomes increasingly important due to environmental problems which we have to face in the future. There are different routes for improving existing technologies, often involving engineering efforts. However, fundamental science also has to provide a contribution, since the optimization of existing technologies has its limitations and understanding of the fundamental physical effects, which leads to the functionality of certain materials, is crucial in order to exploit new routes of optimization. Another frequent problem in optimization is that materials used for laboratory applications often comprise expensive or toxic elements, which are not suitable for industrialization. Consequently, performance improvement of cheap and environmentally friendly materials allows for the exploitation of new applications, which can otherwise not be commercialized.

The following manuscript reports about the investigations of functional iron compounds with respect to their magnetism and lattice dynamics. All the contained elements in these compounds are abundant and non-toxic. The iron content of these materials gives access to measurement methods utilizing the ^{57}Fe nuclear resonance. These powerful microscopic methods allow one to study the nuclear parameters of the materials and their lattice dynamics. Even the electronic parameters are accessible indirectly. The comparison to macroscopic measurements often leads to a deeper understanding of the observed effects.

The investigated materials in this manuscript are interesting for different reasons. The studied FeNCN compound was recently synthesized for the first time and can be seen as a synthetic analogue to FeO. It was reported that the magnetic order temperature of FeNCN, close to room temperature, is higher as that of FeO. Fundamental studies are necessary in order to explain the mechanism responsible for an increase of the transition temperature and may provide a general conclusion for similar materials. The magnetocaloric material $MnFe_4Si_3$ exhibits only a moderate magnetocaloric effect but has a negligible volume change at the transition temperature. This observation is rather unusual for magnetocaloric materials. Consequently, this solid solution can be produced as single crystals, giving access to more characterization methods and thus to a larger information yield than possible for polycrystalline samples. The investigated nanomaterials are studied with respect to their reduced magnetic moment and the unique magnetic properties, which are essential for their applications. Here, the methodological improvement is the main issue and the study of the new results obtained with these techniques.

1.2 Elasticity and Lattice Dynamics

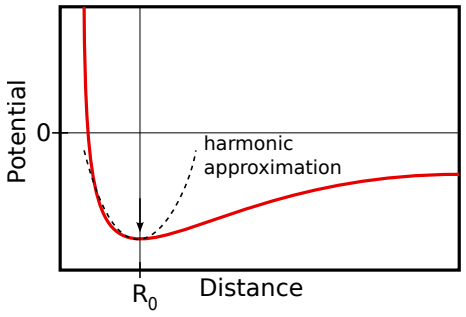

Figure 1.1: Sketch of the atomic potential and the harmonic approximation.

The bonds between atoms in a solid lead to a more or less stable arrangement forming the crystal lattice. The interaction between these atoms can be expressed for any bond type, *e.g.*, covalent, ionic or Van-der-Waals, with a potential as exemplary illustrated in Fig. 1.1. The bond distance R_0 refers to the stable equilibrium state, defined as the energetic minimum of the whole system.

An externally induced distortion of this equilibrium state leads to a response of the lattice and can be described in two different approaches. At the macroscopic scale the solid can be described as a continuum. Consequently, the single atom movements can be neglected and an averaged behaviour of volume elements is studied. The resulting effects are expressed in terms of elasticity and compressibility of the solid. In a microscopic description, the approach has to consider the lattice structure and the single atom displacement, leading to a description in terms of phonons as quantized lattice vibrations.

Elasticity

The elastic deformation of a solid in macroscopic scale is described with the generalized Hooke's law $\sigma = c\epsilon$. The formula describes the linear relation of the strain ϵ, defined as relative length variation, with the applied stress σ, defined as force per area, with the elastic modulus c, also referred to Young's modulus. The matrix form is[1,2]:

$$\sigma_{ij} = \sum_{kl} c_{ijkl}\epsilon_{kl}. \tag{1.2.1}$$

The tensor c_{ijkl} is a tensor of fourth rank with 81 components. The symmetry relations $\epsilon_{kl} = \epsilon_{lk}$, $\sigma_{ij} = \sigma_{ji}$ and $c_{ijkl} = c_{klij}$ allow for reducing the number of components to 21 different elastic moduli[1,2]. However, further reduction can only be obtained under consideration of the crystallographic symmetry. For example, a tetragonal system is describe by a second rank tensor[3]:

$$\begin{pmatrix} c_{11} & c_{12} & c_{13} & 0 & 0 & 0 \\ c_{12} & c_{11} & c_{13} & 0 & 0 & 0 \\ c_{13} & c_{13} & c_{33} & 0 & 0 & 0 \\ 0 & 0 & 0 & c_{44} & 0 & 0 \\ 0 & 0 & 0 & 0 & c_{44} & 0 \\ 0 & 0 & 0 & 0 & 0 & c_{66} \end{pmatrix} \tag{1.2.2}$$

A hexagonal system has the additional constraint $c_{66} = \frac{c_{11}-c_{12}}{2}$.

Starting from these moduli, it is possible to calculate common bulk properties such as the Poisson ratio μ, the bulk modulus B, the shear modulus G or even the sound velocity v_s. The corresponding formulas can be derived for any crystal symmetry. For selected symmetries, the bulk properties can not be directly derived, but rather an average over all crystal directions has to be considered first, as in the hexagonal case. This average can be performed over the stress or the strain, leading to different results. Performing the strain average, a uniform stress in the sample is assumed. This approximation is called Reuss average. The Reuss average always leads to underestimated bulk constants and thus to lower sound velocities and can thus be understood as an approximation for the lower limit. The average over the stress refers to a uniform strain and leads to the Voigt average. This average leads to overestimated constants and can be considered as the upper limit. The corresponding formulas and a detailed description can be found in Ref. (4, 5). However, the bulk properties in higher symmetric structures can be calculated in a straightforward way from the moduli, as for example in the cubic case[3]:

$$\mu = 1/(1 + \frac{c_{11}}{c_{12}}) \tag{1.2.3}$$

$$B = (c_{11} + 2c_{12})/3 \tag{1.2.4}$$

$$G = c_{44} \tag{1.2.5}$$

The longitudinal or transversal sound velocity for the [100] direction of a solid with cubic symmetry and the density ρ is given as:

$$v_s^{long} = \sqrt{\frac{c_{11}}{\rho}} \tag{1.2.6}$$

$$v_s^{trans} = \sqrt{\frac{c_{44}}{\rho}}. \tag{1.2.7}$$

The elastic moduli further allow one to calculate the full body mechanical resonance frequencies of a sample, when the shape of the sample is considered for the calculation. A complete description of the derivation is given in Ref. (3). Here, just a short introduction to the main idea will be given. The resonance frequencies are obtained by minimization of the Lagrangian $L = \int_V E_{kin} - E_{pot}\, dV$ with the kinetic and the potential energy:[3]

$$E_{kin} = \frac{1}{2} \sum_i \rho \omega^2 u_i^2 \tag{1.2.8}$$

$$E_{pot} = \frac{1}{2} \sum_{i,j,k,l} c_{ijkl} \frac{\delta u_i}{\delta x_j} \frac{\delta u_k}{\delta x_l}. \tag{1.2.9}$$

The energies depend on the density ρ, the frequency ω, the ith component of the displacement u_i and the elastic moduli c_{ijkl}. The derivation of this formula leads to the elastic wave equation connecting certain frequencies with the elastic moduli:

$$\rho \omega^2 u_i + \sum_{j,k,l} c_{ijkl} \frac{\delta^2 u_k}{\delta x_j \delta x_l} = 0. \tag{1.2.10}$$

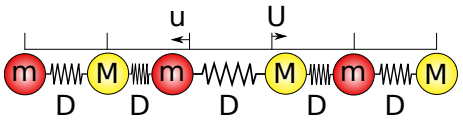

Figure 1.2: Sketch of a diatomic linear chain with masses m and M, corresponding displacements u and U and spring constant D.

Lattice Dynamics

A microscopic description of lattice deformations is obtained by analysing displacements of atoms. For this purpose, the example of a diatomic linear chain is used in order to describe the basic derivation, whereas for complex three dimensional structures the procedure can be performed similarly. The system is sketched in Fig. 1.2. The coupling constant D between the atoms describes the linear interaction strength due to the approximated harmonic potential, as sketched in Fig. 1.1. The corresponding equations of motion with periodic boundary conditions are:

$$m\frac{d^2u}{dt^2} = D(U_{(n)} - u_{(n)}) + D(U_{(n-1)} - u_{(n)}) \tag{1.2.11}$$

$$M\frac{d^2U}{dt^2} = D(u_{(n)} - U_{(n)}) + D(u_{(n+1)} - U_{(n)}) \tag{1.2.12}$$

with the displacement u of the atom with mass m and U of the atom with mass M. The index n indicates the position of the corresponding atom. Solving these equations with the ansatz of plane waves with frequency ω and wave vector q leads to the dispersion relation:

$$\omega^2 = D\left(\frac{1}{m} + \frac{1}{M}\right) \pm D\left[\left(\frac{1}{m} + \frac{1}{M}\right)^2 - \frac{4}{mM}\sin^2\frac{q}{2}\right]^{\frac{1}{2}}. \tag{1.2.13}$$

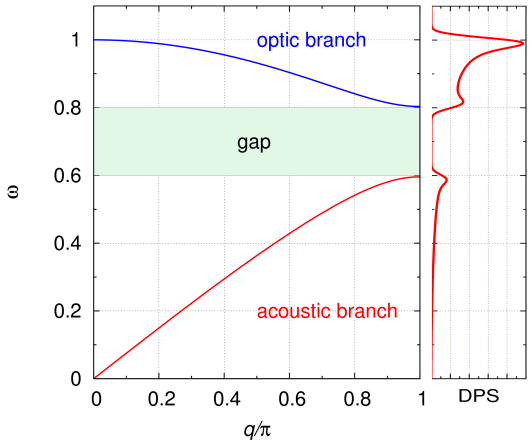

Figure 1.3: The dispersion of a diatomic chain in the first Brillouin zone (left) with the corresponding density of phonon states (right).

The obtained dispersion relation is illustrated in the first Brillouin zone in Fig. 1.3. The gap between the optical and the acoustic branch is caused by the difference of mass m and mass M. The dispersion relation links the wave vector to the corresponding energy, represented in terms of frequency, and thus describes the possible oscillation modes of the lattice. For example, the optical

branch describes modes where m and M oscillate with opposite phase[6]. Only the acoustic branch exhibits a linear relation for small q and thus a constant group velocity of the modes. The group velocity is generally related to the dispersion via[6]:

$$v_g = \nabla_q \boldsymbol{\omega}(q). \tag{1.2.14}$$

The number of all oscillation modes is limited in real solids due to the finite size and the periodicity of the crystal lattice. The number of wave vectors per volume can be expressed in dependence of ω. The density of phonon states can be expressed as[6]:

$$D(\omega) = \frac{V}{(2\pi)^3} \int_{\omega=constant} \frac{dS_q}{\left|\nabla_{\boldsymbol{q}} \omega(\boldsymbol{q})\right|} \tag{1.2.15}$$

with dS_q an infinitesimal area element of a surface with constant ω. The DPS is also sketched in Fig. 1.3. For an isotropic 3D material[6], a constant group velocity at small q in the dispersion relation leads to quadratic behaviour of the DPS at small ω. The pre-factor of the quadratic behaviour is thus directly linked to the group velocity. This result can be expanded to non-isotropic solids for small q and thus for small ω, whenever the dispersion at small q can be linearly approximated. Beside the group velocity, different other material properties can be calculated from the DPS as, *e.g.*, mean force constant, internal energy, specific heat or vibrational entropy. The corresponding formulas are given in Ref. (7, 8), derived for the case of element specific DPS as obtained with nuclear inelastic scattering. For example, the sound velocity and the entropy per atom are[7,9]:

$$v_s = \left[\left(\frac{m'}{m}\right) \frac{E^2}{2\pi^2 \hbar^3 n D(E)}\right]^{1/3} \tag{1.2.16}$$

$$S = 3k_B \int_0^\infty D(E) \left[\frac{\beta E}{2} \frac{e^{\beta E}+1}{e^{\beta E}-1} - ln\left(e^{\beta E/2} - e^{-\beta E/2}\right)\right] dE \tag{1.2.17}$$

with m' the mass of the nuclear resonant isotope, m the average atomic mass, n the density of atoms, k_B the Boltzmann constant and $\beta = \frac{1}{k_B T}$.

Combination of Elasticity and Lattice Dynamics

The macroscopic and the microscopic approach of the lattice deformation can refer to the same physical properties as shown for the sound velocity. Also phase transitions can be studied within both approximations[3,6,10]. However, in case of long-wavelength and thus small q the dispersion relation in the microscopic regime can be directly linked to elastic moduli of the macroscopic approach, according to Ref. (10). For example, a wave vector $[k_x, 0, 0]$ can be correlated to the longitudinal acoustic dispersion $\rho\omega^2 = c_{11}k_x^2$ and transversal dispersion $\rho\omega^2 = c_{44}k_x^2$, with ρ the density, in a cubic system[10]. The long-wavelength limit thus refers to the overlap of both approaches, because displacement of lattice atoms with a wavelength in macroscopic scale can be seen as a movement of a volume element. If this volume element is large enough and averaged over a sufficient number of primitive unit cells, the macroscopic description can be used for expressing the equation of motion of this volume element.

1.3 Magnetism

The magnetic moment M of a paramagnetic sample divided by the saturation magnetization M_s can be described in dependence of the applied magnetic field B and the temperature T with the Brillouin function[11]:

$$\frac{M(y)}{M_s} = B_J(y) = \frac{2J+1}{2J}\coth(\frac{2J+1}{2J}y) - \frac{1}{2J}\coth(\frac{y}{2J}) \tag{1.3.1}$$

and the substitution $y = \frac{g_J \mu_B JB}{k_B T}$. The total angular momentum $\boldsymbol{J} = \boldsymbol{L} + \boldsymbol{S}$ with spin $\boldsymbol{S}$, angular momentum $\boldsymbol{L}$, and Landé g-value g_J are defined by the electronic configuration of the atom. The constant μ_B is the Bohr magneton and k_B is the Boltzmann constant. For paramagnetic samples the saturation magnetisation per atom is $g_J \mu_B J$ per magnetic atom. On changing temperature, the magnetisation in small fields exhibits a $1/T$ behaviour, refereed as Curie's law[12]. This behaviour depicts the Langevin paramagnetism, related to localized moments in solids.

In case of conducting materials, *i.e.* with delocalized electrons, a paramagnetic behaviour can arise from the conduction electrons, a phenomenon called Pauli paramagnetism. At zero field, the spins of the conduction band electrons have no preferred orientation leading to a zero net magnetisation. On application of an external magnetic field, the parallel alignment to the external magnetic field will be energetically favourable and the possible energy gain shifts the spin-up and spin-down bands, leading to an imbalance and thus to a net moment. The temperature dependence of this moment can only be described correct within the model of spin fluctuations and thus need material specific simulations[13]. Transition metals exhibit usually a large density of electronic states at the Fermi level and thus a large contribution of the Pauli paramagnetism[6].

On decreasing the temperature, many materials exhibit a magnetic transition from a paramagnetic to an ordered state, since the inter-atomic magnetic interactions become more and more important compared to the thermal excitation. The magnetic interaction can be described generally by the Heisenberg-Hamiltonian:

$$\mathcal{H} = \sum_{i,j} \mathcal{J}_{ij} \boldsymbol{J_i} \cdot \boldsymbol{J_j} \tag{1.3.2}$$

with the exchange constant $\mathcal{J}_{ij}$ and the total angular momentum $\boldsymbol{J_i}$ and $\boldsymbol{J_j}$ of atoms i and j, respectively. This description assumes localized moments and thus localized magnetism. In case of $3d$ ions it is often found that $\boldsymbol{L} = 0$ and $\boldsymbol{J} = \boldsymbol{S}$ due to quenching of the orbital moment by the crystal field[11].

A study of these magnetic interactions in materials, also including interaction with conduction electrons and band magnetism, leads to different effects such as super exchange, direct exchange, indirect exchange, *etc.*. These effects lead to known order phenomena in solids, *e.g.*, ferromagnetism, anti-ferromagnetism, ferrimagnetism or spin-glass behaviour. All these ordered states and the responsible interaction phenomena are elaborated in most textbooks of magnetism[11–13] and will not be discussed here. In the following, selected phenomena and effects, which are useful for the experimental part of the manuscript, will be discussed.

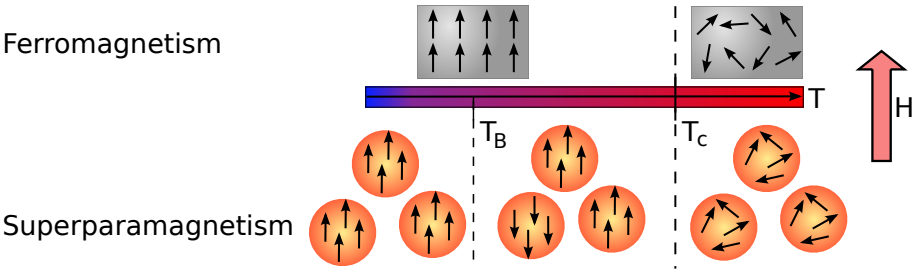

Figure 1.4: Sketch of the superparamagnetic transition of ferromagnetic nanoparticles compared to a normal ferromagnetic bulk.

Superparamagnetism

Materials with nanoscale structures can exhibit different magnetic phenomena compared to the bulk material[12]. In case the nanosized structure is smaller than the usual magnetic domain size in the material, superparamagnetism can be observed. The effect of superparamagnetism is similar to Langevin paramagnetism but a difference appears in the angular momentum J being related to the moment of the nanosized structure instead of a single atom moment.

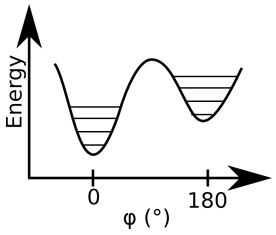

Figure 1.5: Energy landscape of a superparamagnetic system with an angle ϕ between the magnetic moment and the applied magnetic field. At elevated temperatures, the parallel and anti-parallel alignments are possible, whereas they are not equal in energy.

The in-field temperature behaviour of a nanosized ferromagnet in comparison to a normal ferromagnet is illustrated in Fig. 1.4. At high temperatures, if accessible before decomposition, the nanosized material and the ferromagnet exhibit both a paramagnetic phase. On cooling below the Curie temperature, the inter-atomic magnetic exchange and the confinement from the magnetic field is stronger than the thermal excitations, leading to a magnetic order. The ferromagnet exhibits thus an parallel orientation of all spins with respect to the magnetic field, if the field is large enough. The spins of the nanomaterial are also oriented parallel with respect to each other within a single particle forming a macro spin J_{macro}. In contrast to the ferromagnet, this macro spin can be orientated parallel or anti-parallel to the field, because the magnetic interaction between different particles is small and thus the thermal excitation can overcome the confinement from the magnetic field. The parallel alignment is energetically favoured, as illustrated with the energy landscape in Fig. 1.5. An investigation of the excitations between different energy levels is reported in Ref. (14). The probability of jumping between both minima and thus to an anti-parallel alignment depends on the temperature T, leading to a jump rate[12]:

$$\tau = \tau_0 \exp\left(\frac{\langle E \rangle}{k_B T}\right) \tag{1.3.3}$$

with $\langle E \rangle$ the averaged energy of the barrier between both states, k_B the Boltzmann constant and τ_0 the inverse ferromagnetic resonance frequency in the demagnetizing field[12]. For nanomaterials in the superparamagnetic state, the aforementioned Brillouin function can be simplified with the assumption $J_{macro} \rightarrow \infty$ yielding the Langevin function[11]:

$$L(y) = B_\infty(y) = \coth(y) - \frac{1}{y} \tag{1.3.4}$$

The Langevin function describes the superparamagnetic behaviour, depending on temperature and applied magnetic field.

On further cooling down in an applied magnetic field, thermal excitations become to small to overcome the energy barrier and the behaviour is dominated by the energy gain of the energy minimum. Thus, the jumping rate decreases and an increasing amount of macro spins align parallel to the field (also sketched in Fig. 1.4). This effect is called blocking of the superparamagnet. In this temperature region, different magnetic ordered states can be observed, *e.g.*, superferromagnetism or superspinglass behaviour, depending on the properties of the nanomaterial and the interaction between the nanostructures.

As a remark to the magnetic transitions of nanomaterials, the critical temperature for a bulk and a nanomaterial with same composition must not be equal, since the nanostructuring can influence this temperature, as reported for magnetite[15]. Furthermore, the common used term "superparamagnetic transition" often refers to the blocking temperature, whereas the blocking is basically not a magnetic transition, but rather a continuous change in the jumping rate, depending on the time scale of the measurement method. The critical transition of nanomaterial is the paramagnetic to superparamagnetic transition.

Magnetocaloric Effect

The magnetocaloric effect (MCE) consists of a reversible temperature change upon application or removal of an external magnetic field and is related to adiabatic demagnetization of the material. The application of a magnetic field to a material lifts the $2J + 1$ fold degeneracy of the magnetic atomic sublevels and thus reduces the magnetic entropy[12]. As the process is adiabatic, the overall entropy stays constant and consequently the lattice entropy is increased. The material is thus heated. The reverse effect, the demagnetization effect, was used in the past in order to reach millikelvin temperatures[12]. However, the MCE is more general than the adiabatic demagnetization and can also include structural changes and other phenomena changing the lattice and the magnetic entropy with opposite sign.

Fig. 1.6 depicts the MCE as a cyclic process. Between step (a) and (b) the application of a magnetic field aligns the spins, decrease the spin entropy and thus increases the lattice entropy. The increased temperature of the sample will be released as heat to the environment, thus decreasing the lattice entropy again (c). This released heat need to be expelled. When the magnetic field is removed, the magnetic entropy increases, thus decreasing the lattice entropy and the temperature of the material. The temperature of the material will be balanced with the environment by draining heat.

The MCE process requires a direct exchange between lattice entropy S_{lat} and magnetic entropy S_{mag}, in order to be as efficient as possible. However, the conduction electron entropy S_{el} can also be influenced, as can be seen in the thermodynamic description of the entropy depending on

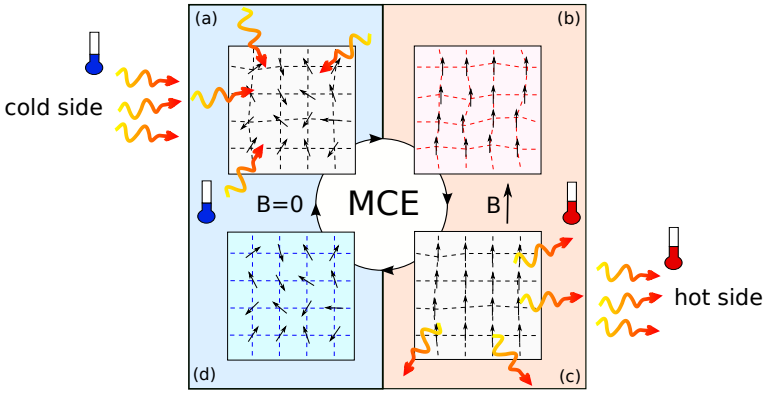

Figure 1.6: Magneto caloric effect depicted as a cycle for cooling application. The exchange between lattice and magnetic entropy is sketched by disorder of the atomic bonds or the magnetic moments.

temperature T, pressure P and magnetic field B:

$$S(T,B,P) = S_{el}(T,B,P) + S_{mag}(T,B,P) + S_{lat}(T,B,P). \tag{1.3.5}$$

Because the entropy change is often measured indirectly by magnetic or heat capacity measurements, the magnitude of the MCE is often overestimated. The determination of the entropy change from magnetometry data depending on temperature and magnetic field can be performed with the following formula, based on the Maxwell relation[16] $\left(\frac{\delta S_m(T,B)}{\delta B}\right)_{T,p} = \left(\frac{\delta M(T,B)}{\delta T}\right)_{B,p}$:

$$\Delta S(T,\Delta B) = \sum_i \frac{M_i(T_i^*,B_i) - M_i(T_i,B_i)}{T_i^* - T_i}\Delta B_i. \tag{1.3.6}$$

The formula is a numerical expression for the derivation of the magnetization M with temperature and the integration over an external applied magnetic field.

Diluted Anti-Ferromagnet

The diluted anti-ferromagnet in a field (DAFF) or uniform magnetic field on a uniaxially anisotropic antiferromagnet (UAAF) with random quenched exchange interaction[17] is a model system used to describe a more or less anti-ferromagnetic state with a significant amount of diluted defects. The defects can be related to distortions, vacancies or impurities, leading to a locally distorted magnetic interaction. For describing the magnetic system, it is possible to apply the random field Ising model with the Hamiltonian[18]:

$$\mathcal{H} = -\sum_{i,j} \mathcal{J}_{ij} S_i S_j - \sum_i H_i S_i \tag{1.3.7}$$

with $S_i = \pm 1$. This Hamiltonian is similar to equation (1.3.2) but with the z component of the spin and extended with a random magnetic field H_i at the position of atom i. As illustrated in Fig. 1.7, the defect influences the orientation of the neighbour atomic moments. On increasing number of defects, the anti-ferromagnetic order becomes more distorted, changing the magnetic behaviour of the sample.

The DAFF system behaves similarly to spin glasses and anti-ferromagnets, *i.e.*, a very small macroscopic moment and splitting of zero-field cooled and field cooled curves. Consequently, it is hard

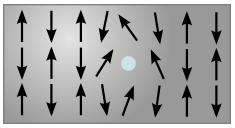

Figure 1.7: Schematic representation of a magnetic system with a defect, influencing the direction of the neighbour moments.

to distinguish the different orders using low magnetic fields. However, in high magnetic fields the ZFC/FC splitting for a spin glass should vanish but still be present for a DAFF system. Typical behaviour of DAFF systems on changing magnetic field and temperature can be found in Ref. (19).

1.4 Nuclear Interactions

The nucleon-nucleon interactions in atomic nuclei lead to different energy states[20], these states can be to some extent described with a shell model similar to the shell model of electrons. In analogy, one can describe the nuclear states with wave functions divided into a radial part and an angular dependent part. In this way one obtains quantum numbers, as known for electrons. One crucial difference between both models is the spin-orbit coupling, which is a correction term for electrons but is in the magnitude of the other quantum numbers for nucleons and can thus strongly influence the energy levels[20].

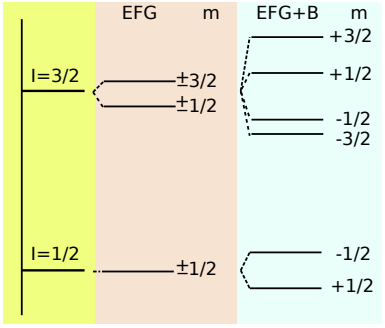

Figure 1.8: Schematic energy levels of the ^{57}Fe nucleus with influence of an electric field gradient (EFG) and a magnetic field (B).

A transition between the nuclear states, such as used for Mössbauer spectroscopy, can only occur with conservation of energy, angular momentum and parity. Solutions of the Maxwell equations within the multipole expansion allow one to describe this process[21]. In what follows, different nuclear hyperfine parameters, which are related to the terms of the multipole expansion of electrostatic interaction, will be discussed with respect to their behaviour on changing conditions as external electric or magnetic fields.

Electric Monopole Interaction - Isomer Shift

The Coulomb interaction between the isotropic part of the nuclear charge distribution[22] and the electronic environment leads to an energy shift ΔE of the nuclear levels[23]:

$$\Delta E = \frac{2}{5}\pi Z e^2 \Delta R^2 \rho(0) \tag{1.4.1}$$

with $\Delta R^2 = R_e^2 - R_g^2$ the difference of the squared radii of the nuclear excited and the nuclear ground state, $\rho(0)$ the electronic charge density at the nucleus and Z the nuclear charge. The chemical environment of the atom (bonds, nearest-neighbours, ...) influences the electronic charge density and thus $\rho(0)$ will differ for different materials. This difference leads, for example in Mössbauer spectroscopy measurements, to an energy shift δ between emitter and absorber:

$$\delta = \Delta E_{abs} - \Delta E_{em} = \frac{2}{5}\pi Z e^2 \Delta R^2 \Delta\rho(0) \tag{1.4.2}$$

with $\Delta\rho(0) = \rho(0)_{abs} - \rho(0)_{em}$ the electronic charge density *difference* of the absorber and the emitter. In order to obtain this equation, some assumptions are necessary, *e.g.*, the nucleus has a spherical shape and the electronic charge density is constant within the nuclear volume. These assumptions are discussed in detail in Ref. (23, 24).

The derived energy shift for different materials allows one to investigate their changing electronic environment due to chemical changes of coordination, bond character or doping[22–24]. For example, Fig. 1.9 depicts different observed isomer shifts for ^{57}Fe depending on coordination and spin. Also the electronegativity and the covalence have an influence on the isomer shift. In all cases, the changing environment of the host atom influences the electron distribution around the nucleus which subsequently changes the electronic charge density at the nucleus position via Coulomb interaction and shielding.

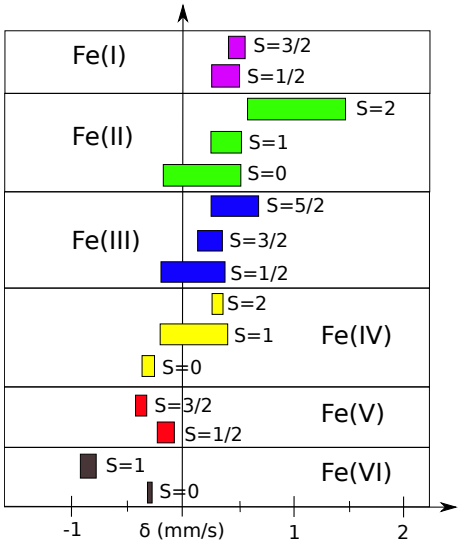

Figure 1.9: Schematic isomer shift for different iron coordination states and different spins. Inspired and data taken from Ref. (22).

The expected isomer shift due to a change in the charge density will be nearly constant upon temperature change, but often a strong change of the measured isomer shift due to the atomic

motion is observed, called second-order Doppler shift. This shift is explained by the relativistic energy shift due to thermal motion of the nuclei[22] and can be described within a Debye model as[22]:

$$\delta_{SOD} = \frac{9k_B E_\gamma}{16 M_{eff} c^2}\left(\Theta_M + 8T\left(\frac{T}{\Theta_M}\right)^3 \int_0^{\Theta_M/T} \frac{x^3}{e^x - 1} dx\right). \tag{1.4.3}$$

M_{eff} is the effective mass of the vibrating atom, E_γ the energy of the photon and T the temperature. The Mössbauer temperature Θ_M is chosen in analogy to the Debye temperature but specific for the sensed environment by the nucleus. The experimentally observed isomer shift is thus the sum of the genuine isomer shift δ and the second-order Doppler shift δ_{SOD}:

$$\delta_{observed} = \delta + \delta_{SOD}. \tag{1.4.4}$$

Electric Quadrupole Interaction - Quadrupole Splitting

The electric quadrupole interaction is the second important term in the electrostatic multipole expansion and describes the interaction of the non-spherical nuclear charge distribution (higher multipolar terms are neglected) with the electric field gradient[24]. The electric field gradient (EFG) arises from a non-spherically symmetric distribution of the surrounding electronic charges, which can be influenced by the bonding character and the crystal structure of solids[24]. The EFG is described by a 3x3 second rank tensor V_{ij}, which is the second derivative of the electric potential V and can be written as[22]

$$V_{ij} = (\delta^2 V / \delta x_i \delta x_j). \tag{1.4.5}$$

This tensor is symmetric and the Laplace equation requires that V_{ij} is traceless, thus only two independent parameters V_{zz}, the principle component of the EFG, and $\eta = \frac{(V_{xx} - V_{yy})}{V_{zz}}$, the asymmetry parameter, are necessary in order to describe the EFG. It is common to choose the principal axis system as the coordination system, such that $|V_{zz}| \geq \left|V_{yy}\right| \geq |V_{xx}|$[24]. The energy of the nuclear magnetic substates, assuming $\eta = 0$, is given as[22]:

$$E_Q(m_I) = \frac{eQV_{zz}}{4I(2I-1)}(3m_I^2 - I(I+1)) \tag{1.4.6}$$

with the spin quantum number I, the magnetic quantum number m_I and the quadrupole moment Q of the nuclear state. As example, the energy difference between the nuclear $I = 1/2$ and $I = 3/2$ states in the ^{57}Fe nucleus, which can be determined in experiments, is given as :

$$\Delta E_Q = \frac{eQV_{zz}}{2}. \tag{1.4.7}$$

In order to discuss the information that can be drawn from the EFG tensor, it is useful to separate the observed energy difference in two contributions, namely the lattice contribution and the valence contribution[22].

The lattice contribution arises from all surrounding charges of the host atom, *e.g.*, the neighbour atoms, impurities or distortions. These charges, which can be considered in first approximation to be point-like, induce a potential V at the host atom and thus influence the EFG according to

formula (1.4.5). However, the electrostatic interaction is not directly transmitted to the nucleus, as electrons of the atom will be polarized, amplifying the effect[22]. Sternheimer[25] introduced an anti-shielding parameter γ_∞ in order to describe this phenomena, leading to:

$$V_{zz}^{lat} = (1 - \gamma_\infty)V_{zz} \tag{1.4.8}$$

$$\eta^{lat} = (1 - \gamma_\infty)\eta \tag{1.4.9}$$

The valence contribution of the EFG describes the direct influence of the valence electrons on the nucleus. The occupied orbitals produce an EFG according to (1.4.5). Since thermal excitation is also possible, a temperature dependence of the EFG is obtained and can be described in a model suggested by Ingalls[26]. Assuming the ^5A state of a Fe(II) high spin atom in octahedral environment with an energy gap Δ due to a trigonal distortion, one obtains:

$$V_{zz} \propto \frac{\sqrt{1 - 2\exp(\frac{\Delta}{k_B T})}}{1 + 2\exp(\frac{\Delta}{k_B T})}. \tag{1.4.10}$$

The energy levels are sketched in Fig. 1.10. The sign of V_{zz} indicates the distortion of the environment and can be used to distinguish the ^5A and the ^5E state. The temperature behaviour of V_{zz} quantifies Δ. Thus the quadropule interaction can be used to investigate the d-orbital configuration.

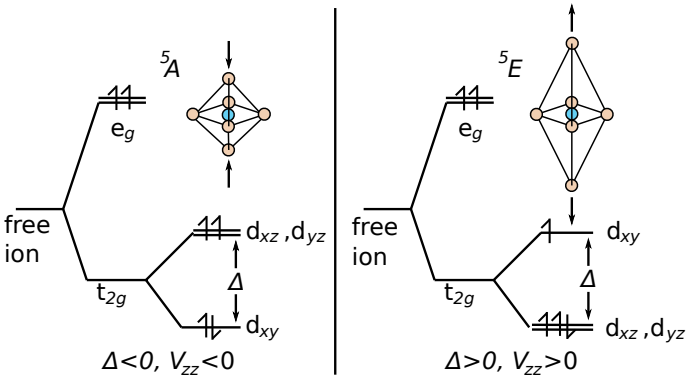

Figure 1.10: Schematic representation of d-orbital levels in an octahedral environment with a trigonal distortion along z. Inspired by Ref. (11, 23)

Comparing the magnitude of lattice and valence contribution to the quadrupole interaction leads to the conclusion that the $1/r$ relation of the electric potential with the distance to a charge, and thus the $1/r^3$ relation of the EFG, indicates that the valence contributions are commonly larger than the lattice contribution.

Magnetic Dipole Interaction - Hyperfine Magnetic Field

The magnetic dipole interaction describes the interaction of a nucleus with a spin quantum number $I > 0$ with a magnetic field B. The energy eigenvalues of this interaction are[22]:

$$E_M(m_I) = -g_N \mu_N B m_I \tag{1.4.11}$$

with g_N the Landé factor and μ_N the nuclear magneton. This interaction lifts the degeneracy of the states $|I, m_I\rangle$[22]. The possible transitions between these states can be found with selection rules for dipole transitions: $\Delta I = 1$ and $\Delta m = 0, \pm 1$.

The magnetic field at the nucleus, generating this splitting, can be considered as an effective magnetic field comprising different terms. As for the quadrupole interactions, it is common to separate the magnetic field in two different contributions. The first contribution arises from the environment of the host atom, as neighbouring atoms or external fields, and is called internal magnetic field. It can be expressed as[23]:

$$B_{int} = B_0 - DM + 4\pi/3M. \tag{1.4.12}$$

B_0 is the external applied field, D the demagnetization factor and M the magnetization of the surrounding volume of the host atom. The demagnetization factor depends on the shape of the investigated volume, *e.g.*, $D = 4\pi/3$ for spherical particles and $D = 0$ for a thin foil[23]. Obviously, the internal field can be easily zero for spherical particles without external applied field. The second contribution to the effective magnetic field is called hyperfine field[23] and comprises the magnetic fields produces by electronic states of the host atom:

$$B_{hf} = B_S + B_L + B_D. \tag{1.4.13}$$

The first term, often the largest one, is the Fermi contact term and describes the interaction of the nucleus with the spin density at the nucleus position. As all core s-electrons are paired, no contribution from this term would be expected. But the spin density of the s-electrons is influenced by polarization of the d- or f-orbitals. This contribution is often approximated with 11 T per unpaired spin for the ^{57}Fe atom *with a negative sign*. The second term is the orbital momentum interaction of the electrons with the nucleus. This term can be expressed as[24]:

$$B_L = -2\mu_B \left\langle r^{-3} \right\rangle \langle L \rangle \tag{1.4.14}$$

with $\left\langle r^{-3} \right\rangle$ the expectation value of the distance and $\langle L \rangle$ the expectation value of the orbital momentum. The third term in the hyperfine field describes the dipolar interaction of the nucleus with the electrons. Usually, the same distribution of the dipolar interaction and the EFG can be assumed, as both effects originate in the partial filled outer shells of the atom. Consequently, the dipolar interaction can be described as[24]:

$$|B_D| = \mu_B V_{zz}/e \tag{1.4.15}$$

The sign and direction of the two latter terms need to be determined for every material individually. As already mentioned, the Fermi contact term will be in most cases anti-parallel to the spin of the host atom. Often, but not mandatorily, the dipolar term and the orbital momentum term are in the opposite direction and way smaller than the Fermi contact term.

Mössbauer Effect - Nuclear Resonant Absorption

The considered nuclear interactions are present in all nuclear absorption and transition processes. However, in order to observe these states in practice, it is necessary to have a recoil free absorption or emission, otherwise the gamma quanta energy is changed, due to the momentum and energy transfer, to[22]:

$$E_\gamma = E_0 - E_R \approx E_0 - \frac{E_0^2}{2Mc^2}, \tag{1.4.16}$$

where $E_0 = E_e - E_g$ is the energy of the nuclear transition defined by the energy of the excited state E_g and the energy of the ground state E_g. E_R is the averaged energy transferred to the atom due to recoil. The expression of the recoil energy, in the non-relativistic approximation, depends on E_0, the mass of the nucleus M and the velocity of light c[22].

In a solid, the nucleus is bound to its neighbours and thus not able to move freely. Consequently, the transferred recoil energy is strongly reduced due to the large mass of the whole system. But phonons can also lead to additional momentum transfer and thus to energy transfer. This process can be described quantum mechanically. It is found that a non-zero probability f exists that describes the zero-phonon process and thus the recoil free fraction[22]. This f factor is called Lamb-Mössbauer factor and can be expressed in dependence of the mean local displacement $\left\langle x^2 \right\rangle$[22]:

$$f = \exp\left(\frac{-\left\langle x^2 \right\rangle E_\gamma^2}{h^2 c^2}\right) \tag{1.4.17}$$

A temperature dependent description of the Lamb-Mössbauer factor can be obtained using the Debye approximation for the density of phonon states with the Debye temperature θ_D[22]:

$$f(T) = exp\left(\frac{-3E_\gamma^2}{k_B \theta_D M c^2}\left[\frac{1}{4} + \left(\frac{T}{\theta_D}\right)^2 \int_0^{\theta_D/T} \frac{x}{e^x - 1} dx\right]\right) \tag{1.4.18}$$

The constant k_B is the Boltzmann constant. As pointed out in Ref. (22), the f factor can be increased with decreasing E_γ, decreasing temperature, or increasing Debye temperature. In practice, θ_D and E_γ are given by the sample and the resonant nucleus and thus only T can be changed in order to increase the obtained recoil free emission or absorption.

1.5 Scattering

The scattering of particles and waves is the underlying effect of different material characterization methods. The different methods base on different scattering phenomena as coherence or incoherence, elastic or inelastic scattering and liner or non-linear scattering. However, this section will rather focus on only one scattering process, namely the elastic-coherent scattering, in order to achieve a description of the small-angle scattering process and compare it to the common Bragg scattering.

The general coherent scattering formula describes the scattering amplitude as the Fourier-transformation of the scattering potential $V(\boldsymbol{r})$[27]:

$$A(\boldsymbol{Q}) \approx \int V(\boldsymbol{r})\, e^{i\boldsymbol{Q}\boldsymbol{r}} d^3 r \tag{1.5.1}$$

The derivation of this formula assumes plane waves, Fraunhofer-approximation and Born-approximation[27]. The scattering angle $|\boldsymbol{Q}| = |\boldsymbol{k'} - \boldsymbol{k}| = \frac{4\pi}{\lambda} \sin\alpha$ is defined by the incoming wave vector $\boldsymbol{k}$, the scattered wave vector $\boldsymbol{k'}$ and the angle α between them. The wavelength of the incoming and the scattered wave is λ. The observed intensity $I(\boldsymbol{Q})$ is the square of the scattering amplitude $A(\boldsymbol{Q})$. The scattering potential depends on the interaction taking place in the scattering process, the outcome of the experiment can thus be described by expressing the correct potential.

Bragg Scattering

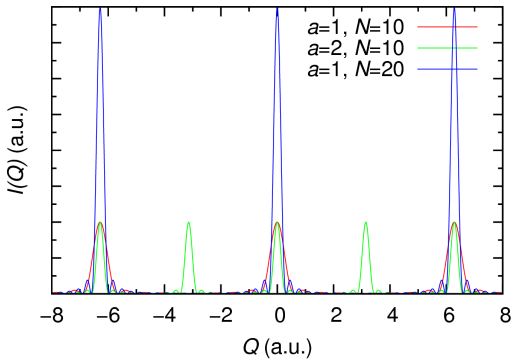

Figure 1.11: Schematic representation of the intensity according to formula (1.5.2).

Bragg scattering can be described by assuming a periodic structure with a certain scattering geometry. By comparing the wavelength differences for different scattering events in the periodic structure it is found that constructive and destructive interference appears, depending on the observer position due to the periodicity of the lattice.

Considering formula (1.5.1) and assuming a finite one-dimensional periodic structure with N scatterer and distance a between them, the scattering potential can be described as:

$$V(r) \approx \sum_{n=0}^{N} \delta(r - na). \tag{1.5.2}$$

Solving the Fourier-transformation for the δ-function and summing up the series leads to[27]:

$$I(Q) \approx |A(Q)|^2 \approx \frac{\sin^2 1/2NQa}{\sin^2 1/2Qa} \tag{1.5.3}$$

The result describes the oscillating scattering pattern in Q observed in an experiment, as depicted in Fig. 1.11. A change of distance a leads to a change of the periodicity but not of the peak position. An increase in the number of scatterers has no influence on the periodicity but the intensity increases and the peaks become sharper. Consequently, the patterns are characteristic for the periodic structure.

Small-Angle Scattering

In a similar way, it is possible to derive the scattering intensity expected for small-angle scattering by small structures. In case the structure and thus the number of scatterer N becomes large (but still finite) compared to the distance a, it is convenient to neglect the effect of Bragg scattering. This assumption can be introduced in the scattering formula (1.5.1) by assuming the potential $V(\boldsymbol{r})$ being constant within a selected region. As an example, the small-angle scattering from a hard sphere can be obtained by assuming the potential $V(\boldsymbol{r}) = V_0$ being constant for $r < R_0$ with R_0 the sphere radius. For larger values of r the potential is assumed to be zero. It follows:

$$I(\boldsymbol{Q}) = |A(\boldsymbol{Q})|^2 = \left| \int_{r<R_0} V_0 \, e^{i\boldsymbol{Q}\boldsymbol{r}} d^3r \right|^2 \tag{1.5.4}$$

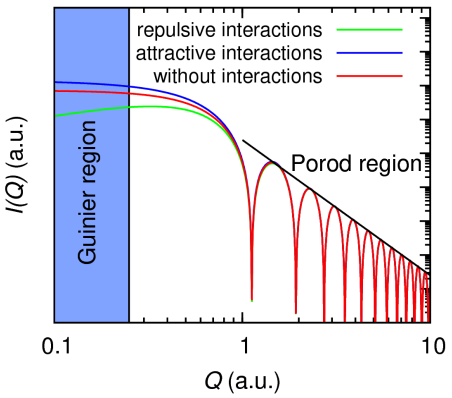

Figure 1.12: Schematic representation of the intensity according to a spherical form factor without and with interactions.

Solving this equation leads to[28]:

$$I(Q) \approx \left| \frac{3V_0}{(R_0 Q)^3} \left[\sin(QR_0) - QR_0 \cos(QR_0) \right] \right|^2 \tag{1.5.5}$$

This scattering amplitude is called hard sphere form factor, plotted in Fig. 1.12. Similar calculation can be performed for arbitrary shapes leading to different form factors. Strictly, this formula holds only for scattering of single particles but in experiments often a dispersion of particles is used. The statistical distribution of particles leads to a second term in formula (1.5.4), the structure factor. In order to solve the equation one has to assume a distribution function of the particles. However, the general influence from the structure factor can be described qualitatively[28]. The effect on the scattering curve is significant only at low Q and vanish for increasing Q. The scattering at low Q will be reduced in case of repulsive interactions and increased in case of attractive interactions[28], also sketched in Fig. 1.12.

Another effect on the scattering by an ensemble of particles, which needs to be considered, is the case of different sizes of these particles. The form factor $A_{sphere}(\boldsymbol{Q}, r)$ for a single sphere with radius r need to be corrected with a distribution function $D(r, R_0)$ with R_0 the averaged effective radius:

$$A_D(\boldsymbol{Q}) = \int_0^\infty A_{sphere}(\boldsymbol{Q}, r) D(r, R_0) dr \tag{1.5.6}$$

In experiments, the shape of the particle and thus the form factor $A_{sphere}(Q, r)$ is assumed to be known and the distribution function is adjusted to the measured scattering pattern. The size distribution does not change the position of the minima and maxima in small-angle scattering pattern, but rather smears out the minima. Consequently, a large size distribution can lead to vanishing of the minima and maxima.

In case of different particle shapes, also a shape distribution can be introduced in formula (1.5.5) in similar way as done for the size distribution. But the adjustment can become to complex and instable with different sizes and shapes and thus the analysis of small-angle scattering pattern should be performed under usage of invariants. The first invariant is found by a Guinier plot, defined as $\ln I(Q)$ against Q^2[28]. The slope of the linear part at low Q^2 has to be $R_g^2/3$ with R_g the radius of gyration. In case the shape of the particles is known, an averaged size can be

determined, *e.g.*, $R_g^2 = \frac{3}{5}R^2$ for the radius R of a sphere[28]. This approximation is only valid in range $Q^2 < (1/R_g)^2$, also illustrated in Fig. 1.12.

The Porod law describes the asymptotic behaviour at larger Q, indicated with the black x^{-4} line in Fig. 1.12. The general asymptotic behaviour of small-angle scattering of particles with a smooth interface is defined as $I(Q) \approx Q^{-4}$. For homogeneous particles the proportionality constant in this formula is linear with the surface of the particle and the scattering potential squared[28]. In this approach another invariant can be obtained, the Porod invariant, given as[28]:

$$P = \int_0^\infty Q^2 I(Q) dQ. \tag{1.5.7}$$

The Porod invariant is related to the volume V of a homogeneous particle via $P \approx 2\pi^2 V_0^2 V$[28].

1.6 Resistivity

The electric conductivity is defined as the proportionality constant between the electric current density and the applied electric field $\boldsymbol{J} = \sigma \boldsymbol{E}$. The resistivity is the inverse conductivity $\rho = 1/\sigma$. The Sommerfeld model for metals defines the conductivity as[6]:

$$\sigma = \frac{ne^2 l}{m v_F} \tag{1.6.1}$$

with the mean free path l, the Fermi velocity v_F, the electron charge e, the mass m and the electron density n. The mean free path is the average distance travelled by an electron before scattered. The Fermi velocity is the corresponding velocity of electrons with Fermi energy. Electrons with much lower energy can not be scattered, because no unoccupied states, which they could fill, exist[6]. The formula expresses the conductivity as a process limited by the mean free path and thus by scattering events. The scattering centers are phonons, defects, impurities, or the surfaces. The temperature behaviour of the resistivity in this model is depicted in Fig. 1.13.

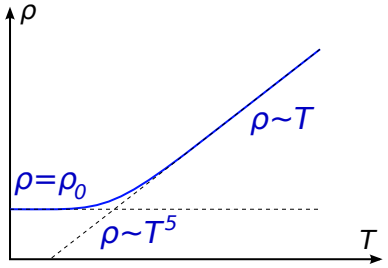

Figure 1.13: Temperature dependent resistivity of metals. The constant resistivity ρ_0 at low temperatures is caused by scattering at distortions. For increasing temperature, phonon terms become more and more important for scattering processes. The illustration is inspired by Ref. (6).

Above the Debye temperature ($T >> \Theta_D$) of the metal, the scattering events are linked to the number of phonons N. Here, N is proportional to T, and consequently the resistivity will linearly increase with temperature. Below the Debye temperature ($T << \Theta_D$), the resistivity will exhibit a

T^5 behaviour due to a T^3 dependence of the phonon number N with temperature and an additional limitation from the possible range of momentum transfer with T^2 dependence.

The T^5 behaviour at low temperatures can be influenced by other effects such as phonon umklapp scattering and phonon drag. A short discussion about both effects can be found in Ref. (29) and will not be given here. Also the Kondo effect[11], describing the influence of magnetic impurities on the resistivity at low temperatures, will not be discussed here.

The scattering by impurities and distortions basically exhibits no temperature dependence, since the number and distribution of scattering centers do not change on changing temperature[6]. However, in case the mean free path becomes bigger than the investigated sample, *e.g.*, the transport becomes ballistic, the scattering at the surface has to be considered, also not changing with temperature. These temperature-independent effects lead to a constant resistivity at low temperatures.

1.7 Measurement Methods

1.7.1 Vibrating Sample Magnetometry

A magnetometer determines the magnetic moment of the whole sample, which is the sum of the single atomic moments. The sample is moved through pickup coils inducing an induction voltage in the coils, which in turn leads to a current. Only the projection of the oscillating moment in the direction of the coils is monitored in this way. The processing of the current in the electronics depends on the specific instrument. In case of vibrating sample magnetometer, the Lock-in amplifier technique is used in order to cope with the small current produced by usually milligrams of magnetic materials. For this purpose, the sample is vibrated with frequency f modulating the induction with the same frequency.

The used sample holder for such a measurement depends on the sample. For powder or crystals, usually gelatin capsules and wool are used, fixed in a plastic straw. The additional materials in the pickup coils lead to an additional, small diamagnetic contribution. In case of liquid samples, a Vespel (polyimide) holder sealed with Teflon tape can be used. This liquid sample holder gives also a small diamagnetic contribution.

Depending on the sample, the cooling procedure can influence the measured results. For example nanoparticle measurements are performed within different cooling procedures, namely zero-field cooled (ZFC) and field cooled (FC) procedure. In case of ZFC procedure, the sample is cooled down to the lowest measured temperature without external magnetic field and then measured with applied field upon *heating*. In FC procedure, the sample is cooled down within an applied magnetic field and measured upon *heating* with the same field.

1.7.2 Mössbauer Spectroscopy

Mössbauer spectroscopy is based on the resonant absorption of gamma radiation without recoil. The radiation is produced by the same nuclear transition as present in the absorber. A detailed description of the technique and related topics can be found in Ref. (22–24) and a typical setup is depicted in Fig. 1.14.

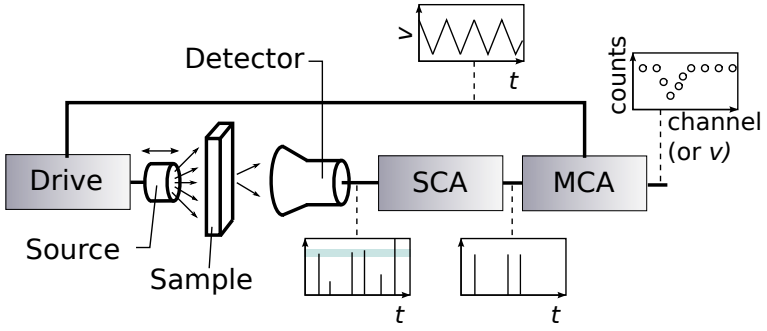

Figure 1.14: Common Mössbauer setup with single channel analyser (SCA) and multi channel analyser (MCA). The signal at selected steps of recording is depicted as insets, whereas t indicates a plot over time and v indicates a plot of the velocity.

The radioactive source emits γ-quanta depending on the nuclear transition. The energy spread of the recoil free quanta is sharp, about 5 neV or 98 ns for the 14.4 keV transition of ^{57}Fe. The energy of the quanta can be changed by the Doppler effect with a drive performing a constant vibration. The nuclear resonant transitions in the sample can be excited by matching the emitted energy with the Doppler shift to the transition energy of the sample. These energies are in range of $\approx$ 1000 neV for ^{57}Fe. The detector counts all photons which are transmitted through the sample. Due to the energy resolution of the detector the single channel analyser (SCA) can resolve pulses arising from the desired transitions with $\approx$ 1 keV resolution and exclude others. But, the energy resolution of the detector is of course too low to separate non-recoil free photons from recoil free photons and thus both are counted as signal. The multi channel analyser saves the incoming signal from the SCA into a memory array. This array is defined by the incoming signal from the drive and comprises one period of the drive. Consequently, every array element can be directly related to the velocity of the emitter and thus to the energy shift of the quanta leading to this number of counts. The obtained spectrum is usually represented as counts against elements of the array, with a suitable reference sample, often α-Fe, the data can be calibrated to velocity instead of array elements.

The counts of the non-recoil free photons exhibit no dependence on the drive velocity in the recorded signal, leading to constant background in the signal. In contrast, the number of counted recoil free photons exhibits a minimum at velocities fulfilling the resonance condition and thus leading to the transition spectrum. The analysis of the obtained data under consideration of the peak shape, size and position can be carried out with various models and software. A mathematical description of the relation between the physical properties presented in section 1.4 and a recorded spectra can be found in Ref. (30).

In practice, some measurement requirements have to be considered. First of all, the sample thickness should be chosen such as the signal to noise ratio is maximized. For thin samples, the electronic absorption is dominating over the resonant absorption and the ideal thickness lies between one and two electronic absorption lengths[31]. For isotopically enriched samples, the value differs strongly and need to be approximated under consideration of the enrichment. Further, it is a possible that a powder sample exhibits a preferred orientation. In this case, four measurements with the sample inclined at the 54.7° magic angle with respect to the γ-radiation has to be performed and summed up. The procedure is explicitly described in Ref. (32). Samples with a large nuclear

resonant absorption can exhibit a non-Lorentzian line shape and other thickness dependent effects, as reported in Ref. (33). These samples lead to complications for Mössbauer spectral analysis but, as we will see in the next section, they are common for nuclear forward scattering.

1.7.3 Nuclear Forward Scattering

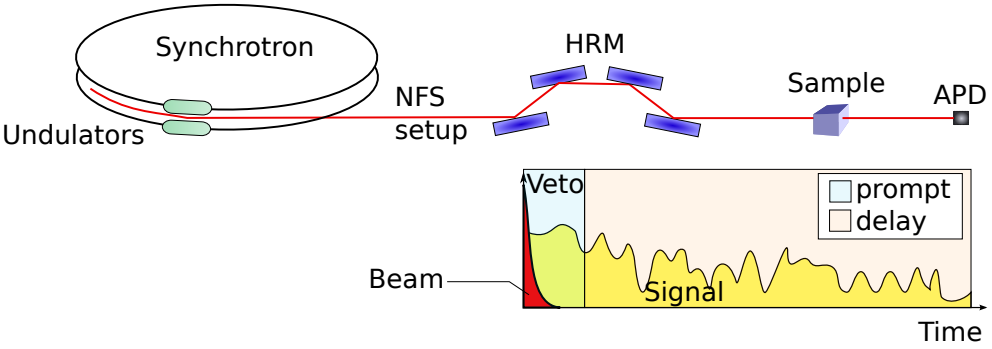

Figure 1.15: Typical setup of nuclear resonance beam line (top). Schematic sketch of NFS data (bottom). The heat load monochromator and additional optics are neglected in the upper picture in sake of simplicity.

Nuclear forward scattering (NFS) is based on the resonant nuclear transitions as well as Mössbauer spectroscopy. But for this technique, the coherent elastic nuclear resonant scattering of photons is measured in time domain instead of the absorption in energy domain. The typical setup for NFS experiments at synchrotron facilities in *pulsed* operation mode is depicted in Fig. 1.15 in a simplified sketch. The energy bandwidth of the incoming synchrotron pulse is strongly reduced with the high resolution monochromator (HRM), *e.g.*, to ≈ 0.7 meV for ^{57}Fe resonant measurements at 14.4 keV, in order to avoid detector overload. The energy bandwidth after the monochromator is obviously much larger than the energy width observed with Mössbauer of 5 neV for ^{57}Fe. However, only the resonant part of the radiation has a large probability to be scattered at the resonant nuclei in the sample. This scattering process changes the temporal evolution of the waves in the sample due to the lifetime of the resonance, in the range of nanoseconds, and the creation of a nuclear exciton[(34)]. Consequently, several nanoseconds after the incoming pulse an out-going intensity signal from the sample is detected. In contrast, the non-resonant photons of the incoming beam are transmitted without any delay as a prompt pulse. The obtained signal over time can be categorized as prompt and delayed signal using an avalanche photo diode and counting electronics.

A schematic sketch of the time evolution of the signal is depicted in Fig. 1.15 - bottom. The measured pattern over time can be understood, on the first glance, as a Fourier transform of the Mössbauer signal, whereas some remarkable effects appear only in the NFS case. For example, the speed-up process leads to a faster decay of the excited state for thicker samples, since the lifetime of the coherent state depends on the density of the nuclear resonant atoms and the thickness of the sample[(34)]. Further for thick samples, purely dynamical beats as additional oscillations in the time spectra are observed due to multiple scattering[(34)].

One of the biggest advantage of NFS as compared to Mössbauer spectroscopy is, next to the small beam size, the full polarization of the beam. The polarization allows one to study direction and

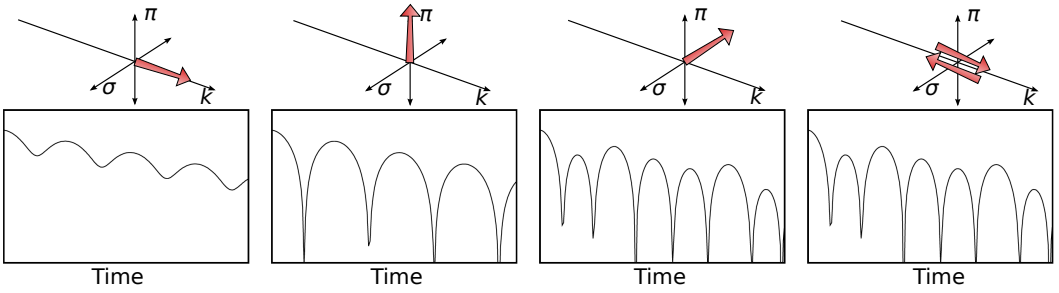

Figure 1.16: Theoretical NFS signal for different directions of hyperfine fields (red arrow) with respect to σ and π polarization of the beam. The wave vector $\boldsymbol{k}$ indicates the beam direction.

magnitude of hyperfine field and electric field gradient in the sample. Fig. 1.16 depicts different arrangements of the hyperfine field with respect to the incoming beam. For different hyperfine field directions different oscillations in the time spectra are present that allow for an analysis of the field direction. Some time spectra can be ambiguous, *e.g.*, two anti-parallel hyperfine fields along the beam give the same time signal as a single hyperfine field along σ polarization. The measured NFS signals are in practice often quite complex and only for selected cases the scattering matrix can be solved directly[34–36]. However, in case of a magnetically split nuclear transitions only and thin sample approximation an analytic expression for NFS amplitudes can be found, as outlined in chapter 4.

1.7.4 Nuclear Inelastic Scattering

Nuclear inelastic scattering (NIS) is an incoherent inelastic nuclear resonant scattering technique and is based on the phonon assisted nuclear absorption[34]. NIS experiments are performed at synchrotrons, as NFS experiments, because the cross section of the process is quite low and thus a high intensity is needed. Furthermore, the photon energy must be shifted in typical phonon range of several meV, not easily accessible with a Doppler drive[34,37].

In NIS experiments, the high resolution monochromator (see Fig. 1.15) is detuned relative to the Mössbauer resonance and thus the resonance condition can only be fulfilled with interaction of phonons in the sample. Assuming the sample to be a randomly orientated powder, any phonon fulfilling the energy conservation $E_{photon} \pm E_{phonon} = E_{transition}$ can be created or annihilated, since in three dimensional powder the momentum conservation will be always fulfilled. The probability of phonon assisted absorption depends on the number of existing phonon states with the particular resonant energy. Consequently, on changing the incoming energy, the density of phonon states (DPS), or more precisely the inelastic scattering function, can be scanned via the absorption process[34,38].

The detection of this phonon assisted absorption process is performed with detection of the decay channels. The excited nuclear state can decay to the ground state with radioactive decay or internal conversion[34]. The internal conversion leads to emission of electrons and following fluorescence. The electron- and photon-emission of the sample can be detected in a large solid angle, as function of the monochromatized energy.

NIS experiments can also be performed on single crystals or not randomly orientated powder. But in case of non-cubic structures, the obtained DPS is a projection on the polarization of the incoming

beam. As pointed out in Ref. (7), the measured absorption efficiency scales with $\boldsymbol{s} \cdot \boldsymbol{e}_j(\boldsymbol{q})$, whereby $\boldsymbol{s} = \boldsymbol{k}/k$ is the unit vector of the incoming beam and $\boldsymbol{e}_j(\boldsymbol{q})$ is the polarization vector of the phonon j. In other words, only phonons involving displacement along the beam are probed.

1.7.5 Resonant Ultrasound Spectroscopy

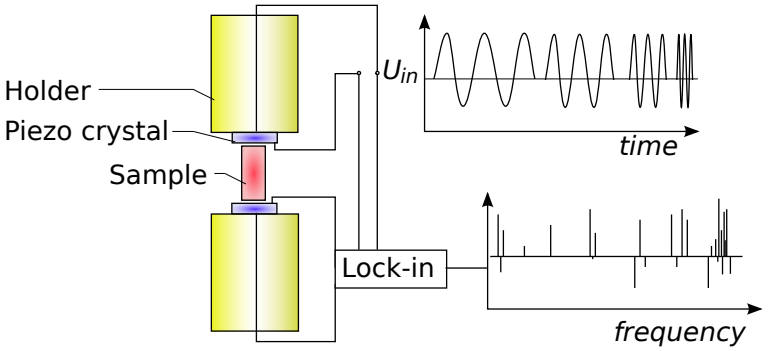

Figure 1.17: Schematical representation of RUS setup. The generated sinus shape signal is applied as pressure waves to the sample via the piezoelectric crystal. The resulting deformation is converted into an electric signal via the second piezoelectric crystal and a Lock-in amplifier. The obtained results are the resonances frequencies of the sample.

A typical setup for resonant ultrasound spectroscopy (RUS) is depicted in Fig. 1.17. An electric signal with changing frequency over time is applied to the upper piezoelectric crystal. The resulting contraction and expansion of the piezo crystal is transmitted as stress to the sample due to the contact. The signal is also transmitted to the lower piezoelectric crystal through the sample and reproduces there an attenuated signal. The attenuation arises mainly from the damping in the sample. But, the sample exhibits different full body resonance frequencies depending on the elastic properties of the material (see section 1.2) and the shape of the sample[(3)]. In case the applied frequency coincides with a natural resonance frequency, the deformation wave will be strongly transmitted to the lower piezo and less attenuated. Consequently, an analysis with Lock-in amplifier technique, in order to improve the signal to noise ratio, can reveal the resonance frequencies of the sample due to the decreased attenuation.

The analysis of the obtained data can be performed with a numerical code, see section 1.2 and Ref. (3). The number of measured resonances strongly influences the accuracy of the fits. A good value found by experience and also mentioned in Ref. (3) is 10 resonances per adjusted parameter. The analyses needs the assumption of the lattice symmetry and quite good starting values, usually elastic moduli of comparable materials are a good starting point.

1.7.6 Resistivity Measurement

The resistivity measurements were performed with the four probe technique in which two current-carrying electrodes and two current free electrodes are used. Commonly, the current free electrodes are placed in between the current-carrying ones and thus exhibit the same potential difference as the corresponding equipotential lines on their position. The resistivity can be calculated with the transmitted current, the voltage drop and the geometry of the sample. The use of four probes instead of two has the main advantage that the wire-resistance can be nearly neglected, because the voltage drop above the (nearly) current-free electrodes is not influenced by the wire resistance

accordingly to Ohm's law $R = U/I$. This setup is particularly necessary for materials with small resistivity.

The sample is usually fixed with non-conducting glue to the sample holder, especially for in-field measurements of magnetic samples. Gold wires used as electrodes are fixed to the sample either with conducting glue or via thermosonic wire bonding. In the following investigations, the former method was used due to the mechanically stronger connection and for the sake of simplicity, because the crystals were sufficiently large.

Chapter 2

2

Magnetism and Lattice Dynamics of FeNCN compared to FeO

Three-dimensional non-oxidic extended frameworks offer the possibility to design novel materials with unique properties, which can be different from their oxide analogues. Here, we present first experimental results concerning unusual magnetic properties of FeNCN, investigated with Mössbauer spectroscopy and magnetometry between 5 and 380 K. This study reveals an unconventional behaviour of the magnetic parameters below the Néel temperature of 350 K, *i.e.*, the hyperfine field on iron decreases with decreasing temperature. At room temperature, quadrupole and hyperfine magnetic field interaction energies are comparable in magnitude, which leads to a rare five-line absorption spectrum. We suggest that these features in the hyperfine field are caused by the combination of a small Fermi contact term and a temperature-dependent contribution from the orbital momentum and the dipole term. One additional spectral component is observed, which exhibits a magnetic relaxation behaviour and slows down at low temperatures to yield a sextet. The magnetometry data suggest that the antiferromagnetic FeNCN is rich in structural distortions, which results in a splitting of the field-cooled and zero-field cooled curves. The lattice dynamics of FeNCN were investigated with nuclear inelastic scattering. The comparison of the obtained data with literature data of iron monoxide reveals very similar iron phonon modes with a small softening and a slightly reduced sound velocity.

M. Herlitschke[1,2], **A. L. Tchougréeff**[3,4], **A.V. Soudackov**[5], **B. Klobes**[1], **L. Stork**[3], **R. Dronskowski**[3], **and R. P. Hermann**[1,2]

[1] *Jülich Centre for Neutron Science JCNS and Peter Grünberg Institute PGI, JARA-FIT, Forschungszentrum Jülich GmbH, D-52425 Jülich (Germany)*

[2] *Faculté des Sciences, Université de Liège, B-4000 Liège (Belgium).*

[3] *Chair of Solid-State and Quantum Chemistry, RWTH Aachen University, D-52056 Aachen (Germany).*

[4] *Independent University of Moscow, Moscow Center for Continuous Mathematical Education, Bolshoi Vlasevsky Per. 11, 119002 Moscow, (Russia).*

[5] *Department of Chemistry, University of Illinois at Urbana-Champaign, Urbana, IL (USA).*

2.1 Introduction

The novel magnetic materials *M*NCN (*M*=metal) are three-dimensional extended frameworks which can be seen as nitrogen containing analogues to the related transition-metal monoxide. In this analogy the NCN^{2-} dianion bridges the metal ions and acts as a diamagnetic ligand supporting the exchange interaction, following the superexchange coupling scenario. The transition-metal monoxides MnO, FeO, CoO and NiO have received much attention in the past due to the origin of their insulating behaviour as Mott-insulators[39] and their antiferromagnetic coupling[40]. Some of these properties are also observed in the corresponding novel non-oxidic frameworks.

The usage of NCN^{2-} as a connecting bridge has a long history, beginning with the fertilizer CaNCN[41]. Investigations of other carbodiimide compounds of alkaline, alkaline-earth metals and other elements followed in the last decades[41]. The investigation of magnetic interactions mediated by such inorganic ligands was initiated more recently. First results were achieved in the field of metal organic frameworks with polymeric metal cyanide compounds, whereby it was found that short bridges (as azido-, cyano- or oxo-bridges) are necessary in order to obtain a strong magnetic coupling between the metal ions[42,43]. Furthermore, magnetic coupling was observed in dicyanamide and tricyanomethanide compounds[42]. In the last decade, different transition metal monoxide analogues bearing the NCN^{2-} bridges were prepared as extended non-oxidic frameworks and characterized structurally and magnetically[41,44,45]. In 2008, the synthesis of FeNCN was reported by Liu *et al.* with first structural and magnetometric investigations[45,46].

FeNCN crystallizes in the $P6_3/mmc$ (194) space group at room temperature, with completely linear NCN^{2-} bridges[46]. The structure can be seen as alternating Fe^{2+} and NCN^{2-} planes (Fig. 2.1). The local environment of each iron comprises six nitrogens, coordinating the iron cation in a slightly distorted octahedron with site symmetry $\bar{3}m$. On the other hand, the carbodiimide is found in a trigonal iron prism with a structural motif that resembles the NiAs type. The corresponding Fe-Fe and Fe-N bond lengths are given in Tab. 2.1. The first susceptibility measurements revealed a Néel temperature of 345 K[45]. The exchange constants obtained by density functional calculations (DFT) indicate a weak ferromagnetic coupling of the spins within the iron plane and a leading antiferromagnetic coupling between adjacent planes[47]. Nonetheless, DFT is notoriously unreliable to find the real ground state, also for FeNCN[48], and DFT exchange parameters have no clear meaning. Many-particle methods are the better choice[49].

Table 2.1: Inter-atomic distances in FeO at 12 K[50] and FeNCN at room temperature[46].

Distance (Å)	FeO	FeNCN
Fe-Fe (same layer)	3.035(6)	3.269(1)
Fe-Fe (adjacent layer)	3.066(6)	4.700(1)
Fe-O / Fe-N	2.15(2)	2.20(2)

For comparison, the analogous iron monoxide has essentially a defect NaCl structure at room temperature, which distorts rhombohedrally along the [111] direction below the Néel temperature, $T_N = 198$ K[52]. The crystal structure at 12 K is $R\bar{3}$ (148)[50]. The magnetic order is ferromagnetic in the (111) planes but antiferromagnetic with respect to neighbouring planes, with moments

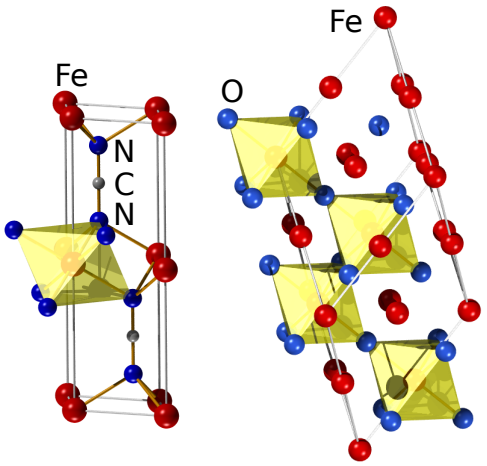

Figure 2.1: Structure of FeNCN illustrated in a $P6_3/mmc$ unit cell (left) and FeO in $R\bar{3}$ (right). The octahedral coordination of the iron is depicted for each Wyckoff position.

Table 2.2: Transition temperatures of metal oxides and the related carbodiimides.

M	M–O^{2-} (K)	M–NCN^{2-} (K)
Mn^{2+}	119 [51]	30 [41]
Fe^{2+}	198 [52]	345 [45]
Co^{2+}	289 [51]	255 [44]
Ni^{2+}	524 [51]	360 [44]

pointing in the [111] direction [52]. Stoichiometric FeO is not stable at ambient conditions and thus always cation deficient. Just as for FeNCN, one can more or less artificially represent FeO as a layered structure in the [111] direction (Fig. 2.1) but containing four different iron sites, with site symmetry $\bar{3}$,$\bar{3}$,$\bar{1}$ and $\bar{1}$, respectively. The local environment of the iron ion is a distorted octahedral coordination by oxygen atoms in each case. The inter-atomic distances for this material are also given in Tab. 2.1. In summary, iron monoxide and iron carbodiimide exhibit a similar local iron environment with a mean nearest neighbour distance of about 2.2 Å in an octahedral coordination by oxygen or nitrogen, respectively. Furthermore, both compounds exhibit a similar antiferromagnetic coupling, although the iron-iron distances between adjacent layers are quite different. It is also remarkable that the Néel temperature of the FeNCN is larger than for FeO. This increase in transition temperature sets the iron carbodiimide apart from the manganese, cobalt and nickel carbodiimide, which exhibit a lower transition temperature as compared to the corresponding oxide (see Tab. 2.2). Furthermore, the Néel temperature is in order of the *d*-shell filling for the oxides but not for the carbodiimides, whose order is broken by FeNCN only. Consequently, stronger exchange interactions might take place in FeNCN or the non-stoichometry in the metastable FeO causes non-uniformity of the magnetic interaction and lead to the lower transition temperature. However, the iron carbodiimide is thus a particularly attractive target for magnetic investigations with Mössbauer spectroscopy and magnetometry.

2.2 Experimental

Sample Preparation

The sample was prepared as described in Ref. (46). In brief, in the first step the reaction of $[Fe(NH_3)_6]^{2+}$ with cyanamide in aqueous solution forms the precursor $Fe(NCNH)_2$. This precursor is air sensitive and must be produced and stored in an inert atmosphere. In the second step, the precursor is decomposed in a halide salt flux at temperatures around 400 °C, thus forming the FeNCN compound plus other by-products. After rinsing with H_2O, the purity was checked with CHN-analysis and XRD.

Mössbauer Spectroscopy

The Mössbauer spectral data were obtained with a spectrometer operating in constant acceleration mode and using a sodium iodide scintillation detector distributed by Ritverc GmbH. Calibration was performed using a room temperature measurement of an α-Fe foil. Around 30 mg of the powder sample were mixed with boron nitride and fixed with tape, for measurements below 300 K, or aluminium foil, for measurements above 300 K, in a titanium sample holder. A small Fe impurity of the aluminium foil was pre-characterized and taken into account in the subsequent data analysis. The sample was mounted in a Janis Research SHI-850-5 cryostat. The temperature steps for the measurement were chosen with monotonic temperature variation in order to avoid hysteresis effects. Representative spectra are depicted in Fig. 2.2. The data were analysed with a program based on the Liouville operator formalism and a stochastic relaxation model[53,54].

Magnetometry

Macroscopic magnetisation measurements were carried out using the vibrating sample magnetometry (VSM) option of a Cryogenic Ltd. closed cycle measurement system. Field-cooled (FC) and zero-field cooled (ZFC) measurements in the range of ±10 T and 5-300 K were recorded. Additional ZFC/FC measurements between 5 and 400 K in range of ±2 T were carried out on the VSM option of a physical properties measurement system (PPMS) distributed by Quantum Design. All presented data were measured upon heating. The sample was prepared as powder.

Nuclear Inelastic Scattering

Nuclear Inelastic Scattering (NIS) measurements[55] enable direct access to the iron specific vibrational modes via the ^{57}Fe Mössbauer resonance. More details about this technique can be found in Ref. (34). The measurements were carried out at beam line P01, PETRA III. Around 12 mg of powderous FeNCN was placed between two tapes. We recorded a NIS spectrum at room temperature. The energy resolution during the experiment was $\approx$ 0.9 meV. The elastic line and the background were subtracted from the measured NIS spectrum, and the iron partial density of phonon states (DPS) was extracted using the program DOS[38].

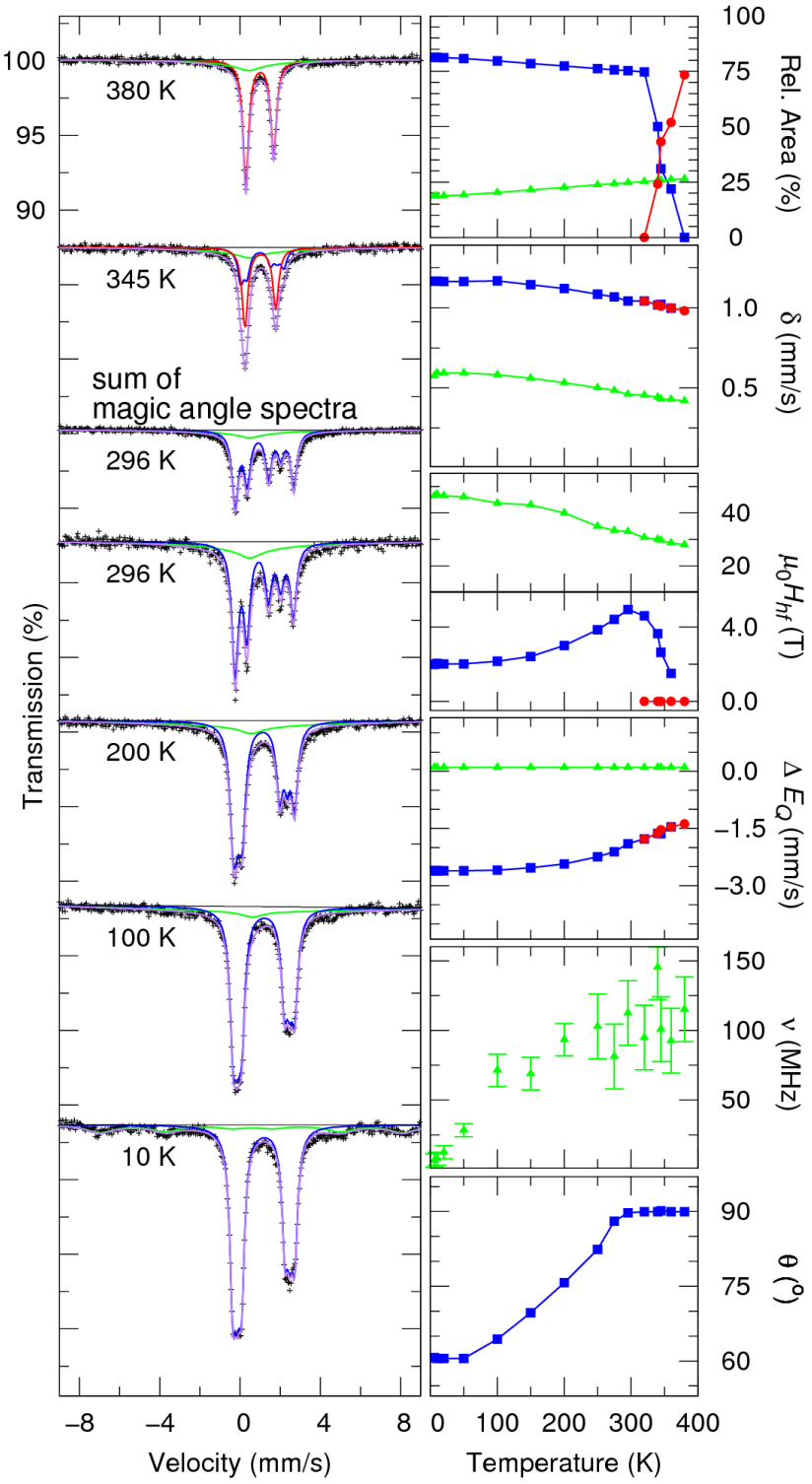

Figure 2.2: Mössbauer spectra of FeNCN at selected temperatures and the extracted parameters from all measurements. The non-relaxing component, attributed to stoichiometric FeNCN, is depicted in blue for the magnetically ordered phase and in red for the paramagnetic phase. The relaxing component is depicted in green and the sum of all components in light purple. Relaxation frequency, ν, and angle, θ, between the hyperfine field and the c axis are plotted only for components with non-vanishing contribution.

Table 2.3: The adjusted parameters from selected Mössbauer spectra. The fixed parameters, according to the description in the text, are given without errors.

	χ^2_{red}		Rel. Area (%)	δ (mm/s)	ΔE_Q (mm/s)	$\mu_0 H_{hf}$ (T)	θ (°)	ν (MHz)
380 K	1.31	I	73(4)	0.98(1)	−1.38(1)	-	-	-
		II	27(4)	0.42(-)	0.1(-)	28(-)	-	115(20)
296 K	1.39	I	75(3)	1.04(1)	−1.90(1)	4.94(1)	90(1)	-
		II	25(3)	0.46(-)	0.1(-)	33.1(-)	-	112(20)
10 K	1.83	I	81(1)	1.17(1)	−2.61(1)	2.04(2)	60.5(3)	-
		II	19(1)	0.59(2)	0.1(1)	47.1(5)	-	9(3)

2.3 Results

Mössbauer Spectroscopy

Prior to modelling, a visual inspection of the Mössbauer data (Fig. 2.2) reveals four distinct regions in terms of temperature dependence. At high temperatures, above 350 K, the material exhibits a paramagnetic doublet. Below the Néel temperature of ≈ 350 K, a five-peak spectrum is observed with a broad background component. Below 275 K, the hyperfine field, $\mu_0 H_{hf}$, of the magnetically split component reduces noticeably from 4.94 T at 296 K to 2.04 T at 10 K. In the last region, below 100 K, the broad component also develops a distinct magnetic splitting.

In order to model the temperature dependence of the spectra, we used a two-component model. One of these components, *i.e.*, the broad one, exhibits a temperature-dependent relaxation process for the magnetic hyperfine interaction, with a relaxation frequency ν. The obtained parameters at selected temperatures are given in Tab. 2.3. In order to improve the stability of the model, the spectra were first fitted with the relative area of the two components as free parameters, and subsequently, we introduced a Debye model[22] for the variation of the relative Lamb-Mössbauer factor. Thus, the relative area in the fit is proportional to the relative amount of the component times the Lamb-Mössbauer factor. Later, the calculated values were used as fixed parameters. The relative areas obtained in the first step and the Debye fit of the second step are depicted in Fig. 2.3. The determined Debye temperatures, or more precisely Mössbauer temperatures Θ_M[22], and the Lamb-Mössbauer factors f_{LM} at room temperature are $\Theta_M = 248(4)$ K and $f_{LM} = 0.51(1)$ for the non-relaxing component and $\Theta_M = 295(30)$ K and $f_{LM} = 0.62(7)$ for the relaxing component, respectively.

The non-relaxing component in the measured spectra, component I, was only adjustable with a model that takes into account a non-zero angle θ between the axis of the largest principal component of the electric field gradient and the hyperfine field for all spectra below 350 K. The angle was estimated to be about 90° at room temperature. Considering the three-fold rotation symmetry along the c axis (Fig. 2.1), it follows that the principal component V_{zz} of the diagonalised electric field gradient tensor must be along c and the asymmetry parameter must be $\eta = \left|V_{yy} - V_{xx}\right| / V_{zz} = 0$. Accordingly, the hyperfine field must be in the ab plane at this temperature. The angle θ decreases with decreasing temperature to $\theta = 60°$ at 10 K. This angle corresponds to the angle between the

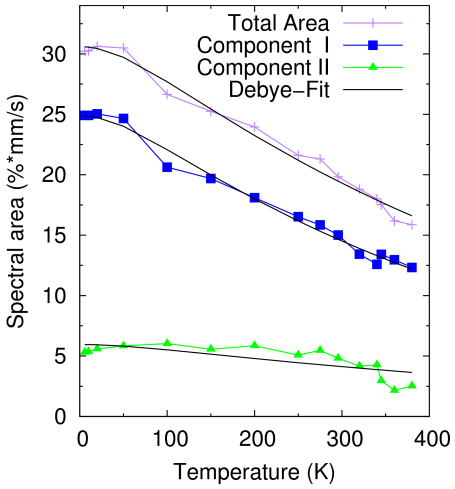

Figure 2.3: The spectral area of the components I and II in the first step of the fitting procedure and the corresponding Debye fits used for the second step.

Fe−N bond and the c axis. Close to the magnetic transition, *i.e.*, above 320 K, the parameter θ needed to be fixed to 90° in order to obtain a reliable adjustment.

At room temperature, an isomer shift, δ =1.04 mm/s, characteristic for high-spin Fe^{2+} is obtained for component I. This isomer shift is thus quite similar to wüstite with $\delta \approx 0.95 - 1.02$ mm/s[56], although the local environment is modified from an oxygen to nitrogen coordination but with similar symmetry. The measured isomer shift is given by the sum of the genuine isomer shift and a relativistic correction, called second-order Doppler shift. The temperature behaviour of the isomer shift was fitted within the Debye model[22]. A Mössbauer temperature for the second-order Doppler shift[22] of 451(30) K was obtained. The observed hyperfine magnetic field exhibits a remarkable behaviour, it increases below the Néel temperature, reaches a maximum at $\approx$ 300 K and then starts to decrease. Furthermore, the maximum at 5 T is also quite small for usual solids. We attribute component I to the stoichiometric FeNCN material. Note that component I shows a slightly broadened linewidth of $\approx$ 0.35 mm/s at all temperatures, a broadening that could indicate small deviations in the local environment of the iron ion.

The broad, relaxing component, component II, features an isomer shift of roughly 0.6 mm/s at 10 K indicating Fe^{3+} or low spin Fe^{2+}. The hyperfine field of 47 T at 10 K is characteristic for Fe^{3+}. It was only possible to extract reliable values for the quadrupole interaction and the hyperfine field of component II below 100 K, due to the smearing effect of the relaxation process and the correlation of the hyperfine field with the relaxation frequency. Above 100 K, the isomer shift for component II was calculated using the Debye model with the Mössbauer temperature extracted from the isomer shift of component I. The hyperfine field was extrapolated linearly and the quadrupole interaction was kept fixed. In the final step, all fits were re-adjusted with the hyperfine field as a free parameter but with a fixed relaxation frequency. In order to verify our modelling of this component, we measured the room temperature spectrum of FeNCN with an enlarged velocity range (Fig. 2.4, top) and found that component II gives contributions to the absorption spectra up to a velocity of ±8 mm/s, which evidences the large area occupied by component II compared to component I.

The used stochastic relaxation model[54] for component II was chosen phenomenologically in order to describe this component, whereby the difference between a relaxation parallel or perpendicular to the electric field gradient can not be resolved due to the quadrupole interaction of ≈ 0 mm/s. A measurement at 6 K with very good statistics of ≈ 6 million counts in the baseline, *i.e.*, roughly ten times the usual number of counts in the baseline of our measurements, reveals some discrepancies with the used model (Fig. 2.4, bottom). These discrepancies could be related to a slightly different relaxation mechanism, some additional distribution of hyperfine parameters or another component.

Both components exhibit texture at all temperatures, *i.e.*, preferential orientation. The texture was verified using a magic angle measurement[32] (see Fig. 2.2). A small discrepancy between the fit and the spectra at about 4 mm/s can be observed at any temperature, possibly related to an incremental increase in the linewidth. We found no indication for this discrepancy to result from an additional component.

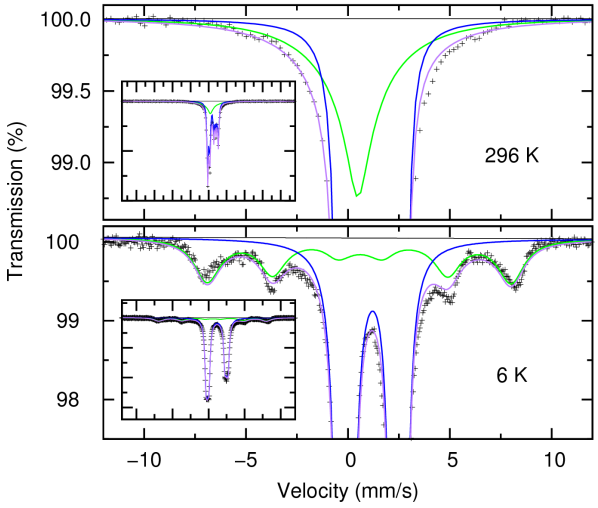

Figure 2.4: Additional spectra of FeNCN at room temperature with enlarged velocity range (top) and 6 K measurement with very good statistics (bottom). The colors are chosen as in Fig. 2.2.

Magnetometry

The ZFC/FC curves at different magnetic fields are plotted in Fig. 2.5a and feature an antiferromagnetic transition close to 350 K, as also observed by Mössbauer spectroscopy. The splitting in the ZFC/FC curves below 350 K for the three different applied fields can be an indication of different magnetic order phenomena. In principle, this splitting could be related to superparamagnetism which would also explain the relaxation behaviour observed for component II by Mössbauer spectroscopy. However, superparamagnetism is ruled out because the splitting also appears at a magnetic field of 2 T and at such high fields the order should vanish. The ZFC/FC splitting could also be related to a spin glass. But, similarly to superparamagnetism, the spin glass is a "weak" magnetic order and a shift in transition temperature with increasing magnetic field, until it vanishes or smears out at high fields[57,58], would be expected. No change in transition temperature was observed and the transition becomes gradually even more pronounced with increasing field. Other frequency dependent order phenomena can also be ruled out, because the transition tempera-

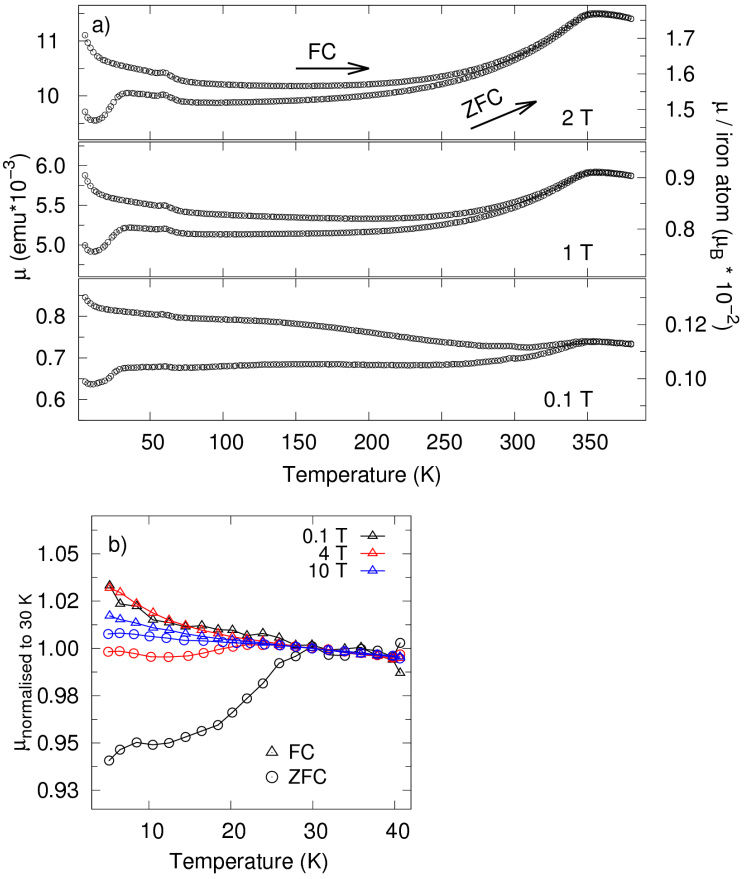

Figure 2.5: Temperature dependence of the magnetic moment μ in FeNCN for ZFC/FC measurements with different magnetic fields. The temperature was varied between 5 and 380 K for (a) and between 5 and 40 K for (b).

tures in Mössbauer spectroscopy and magnetometry are very close and both measurements provide information at very different time scales, ns and s, respectively.

We suggest to attribute the splitting of the curves to distortions in the sample, as reported for YFe_2O_{4-x} [59]. The structural disorder due to distortions or impurities locally destroys the antiferromagnetic order and leads to parasitic ferrimagnetic moments. As a consequence, the moments in the sample will arrange and "freeze" differently on zero-field cooling compared to field cooling, because the introduced parasitic moments align parallel to the applied field and generate completely different starting conditions for the cooling procedures. A microscopic description of similar behaviour can be found for diluted antiferromagnets in a uniform field (DAFF), based on a random field Ising model [17–19]. The interplay of the anisotropy and dilution (impurities) also leads to different behaviour on ZFC or FC.

Another feature of the data in Fig. 2.5a is the small bump at around 60 K. This peak is related to the freezing of oxygen. It was not possible to remove this peak with additional purging. Consequently, there is a strong adsorption of oxygen on the surface, according to our experience.

With respect to component II in Mössbauer spectroscopy two conclusions can be drawn from the magnetometry data: first, there is no remarkable indication for typical oxides, *e.g.*, Verwey

transition for magnetite at 119 K or Néel temperature for wüstite at 198 K. Second, the overall magnetisation up to 2 T is very small and with a contribution of almost 19 % of component II, estimated by Mössbauer spectroscopy, one would expect much higher values considering ferri- or ferromagnetic materials. As a consequence, only antiferromagnetically coupled iron containing compounds or impurities are reasonable for component II.

Beside the Néel transition at 350 K another transition was found only in the ZFC curves in range of 5-30 K, a transition which also features an interesting field-dependent behaviour. ZFC/FC measurements up to 10 T in the range of 5 to 40 K exhibit a splitting between both curves, see Fig. 2.5b. The existence of this splitting up to high magnetic fields indicates a very strong order. This effect may be related to some unreacted $Fe(NCNH)_2$ precursor, which is known to exhibit similar behaviour in low temperature magnetometry (supporting information in Ref.(46)). Furthermore, in Mössbauer spectroscopy we observed a magnetic transition of the precursor from a paramagnetic to an ordered state between 15 and 30 K (detailed investigations will be reported elsewhere). This transition could lead to the observed field-dependent splitting of ZFC/FC curves between 5 and 30 K. $Fe(NCNH)_2$ is not observed in the Mössbauer spectra, but a small amount of ≈ 1 % can not be excluded. Magnetometry might be sensitive to the latter material, because the paramagnetic $Fe(NCNH)_2$ provides a larger signal at low temperatures compared to the antiferromagnetic FeNCN.

Nuclear Inelastic Scattering

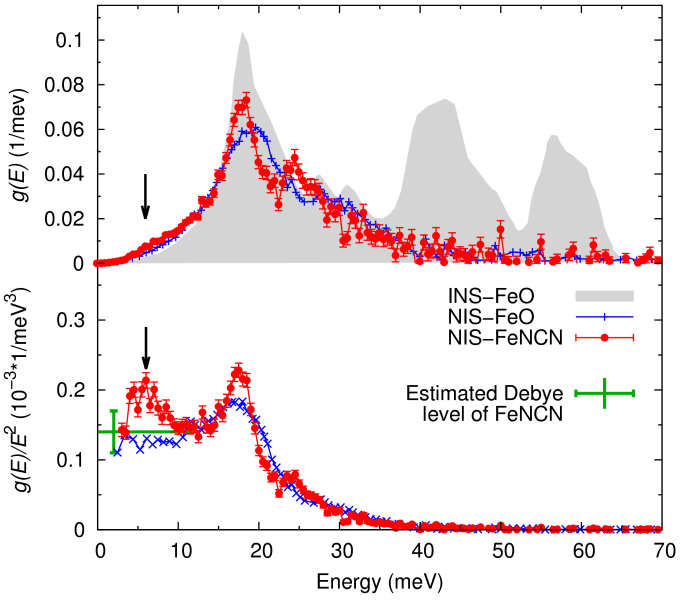

Figure 2.6: Iron specific DPS (top) and reduced DPS (bottom) of FeNCN extracted from NIS measurements at 300 K compared with FeO at 0.9 GPa from Ref. (60). In addition, the total DPS of FeO obtained from inelastic neutron scattering (INS) (Ref. (52)) is highlighted in grey. The region of the subtracted elastic line was omitted in the reduced DPS plot.

The extracted iron specific density of phonon states (DPS) of FeNCN, $g(E)$, is depicted in Fig. 2.6. In both compounds, the iron monoxide and the iron carbodiimide, the major number of iron phonon states is located in the energy region below 40 meV with similar shape in each case. The

maxima of FeNCN are slightly shifted towards lower energy as compared to FeO, which represents relatively softer phonon modes. The features in the FeNCN spectrum are more defined compared to FeO, probably due to a better resolution in our experiment.

In the low energy region, between 4 and 8 meV, the iron carbodiimide features an increased number of phonon states, as seen in the reduced DPS, *i.e.*, $g(E)/E^2$. This bump is specific for FeNCN and not obvious in FeO and might be an indication for glass-like behaviour. The area of the bump compared to the overall DPS is about 0.8(4) %. The Debye level of FeNCN, defined as the low energy limit

$$\lim_{E\to 0} \frac{g(E)}{E^2}, \tag{2.3.1}$$

seems to be slightly increased as compared to FeO. This increase corresponds to a decrease of the sound velocity[9]. The exact determination of the Debye level is quite difficult, due to the presence of the soft phonon mode, the finite resolution and the subtraction of the elastic line. In approximation, one can confine the possible range of the Debye level as highlighted in Fig. 2.6. This range leads to a sound velocity of 3200 m/s ±300 m/s. For comparison, the iron monoxide has a sound velocity of around 3500 m/s as determined by NIS[9]. A list of other parameters calculated using the extracted DPS from the NIS measurement of FeNCN at room temperature is given in Tab. 2.4.

Table 2.4: The calculated values from the iron specific DPS of FeNCN, obtained with the program DOS[38].

Lamb-Mössbauer factor	0.62(4)
Internal Energy	91(10) meV
Mean Force Constant	127(60) N/m

2.4 Discussion

The investigation of the iron carbodiimide revealed some similarities to the metastable iron monoxide, as expected. The isomer shift is comparable to the iron monoxide with the same Fe^{2+} state and a similar AF order appearing at higher temperatures. In contrast, the hyperfine field is strongly reduced from 34 T in the iron monoxide at 77 K[56] to ≈ 2 T for FeNCN.

The second component with a relative contribution of ≈ 19 % in Mössbauer spectroscopy exhibits an isomer shift of 0.6 mm/s and a hyperfine field of 47 T at 10 K. This combination of hyperfine parameters is characteristic for Fe^{3+}. The hyperfine field is in the usual range for iron oxides and hydroxides. The magnetometry data reveal only a small magnetic moment for all temperatures and we found no indication in the magnetometry measurements for this component to be a common oxide (see Fig. 2.5). We assume that component II is an impurity, related to the production or ageing process of FeNCN or the $Fe(HNCN)_2$ precursor. The magnetic order of this impurity at low temperatures indicates a quite stoichiometric material. The overall small magnetisation at low temperatures and high magnetic fields leads to the conclusion of a strong antiferromagnetic

or weak ferri/ferromagnetic coupling. Furthermore, an intrinsic distribution of the Fe^{3+} impurity could explain the splitting in ZFC/FC curves below the Néel temperature.

Another remarkable difference between FeO and FeNCN is an unusual behaviour of the hyperfine magnetic field in component I. Usually, a decrease of the hyperfine field with *increasing* temperature is observed until the hyperfine field vanishes at the Néel or Curie temperature, as indeed observed for FeNCN, but only between 300 and 350 K. Below 300 K the hyperfine field in FeNCN decreases with decreasing temperature. In addition, the angle between the hyperfine field and the quadrupole interaction gradually decreases from 90° to 60° between 300 and 10 K. This change in the angle corresponds to an alignment of the hyperfine field in the *ab* plane at room temperature and a 60° tilting with respect to the *c* axis at low temperatures, assuming the $P6_3/mmc$ structure. The low temperature angle is thus equal to the angle between the Fe−N bond and the *c* direction. Both, the change of the hyperfine field and the change of the angle θ, exhibit a similar behaviour upon changing temperature and thus are likely correlated. In order to improve the understanding of the observed behaviour of component I possible interactions in the material must be discussed in light of the magnetometry results and the antiferromagnetic order at low temperatures.

First, while analysing the Mössbauer data, a magnetic relaxation scenario according to Ref. (53, 54) was tested in order to explain the observed reduction of the hyperfine field of component I. Two facts contradict this hypothesis: the relaxation does not reproduce the correct line shape, *i.e.*, the observed high velocity lines in the low temperature spectra are broader than the low velocity lines but relaxation tends to make them equal. Furthermore, the relaxation frequency would increase on decreasing temperature in contrast to usual observations.

Second, we consider that the magnetic field seen by the nucleus is reduced upon decreasing temperature. The hyperfine magnetic field in absence of an external field is defined as[23]:

$$\mu_0 H_{hf} = B_D + B_L + B_S \tag{2.4.1}$$

with the contributions B_D produced from the dipolar interaction, B_L produced from the electronic orbital momentum and B_S related to the Fermi contact term. The first two terms are usually small in iron compounds[23] and thus we first focus on the Fermi contact term, which describes the interaction of *s*-electrons with the nucleus. Because the *s*-electrons are paired, their contribution is due to their polarization by *d*-electrons and is quite large[25]. Consequently, possible effects of *d*-electron configuration need to be considered as they may change the contribution of the Fermi contact term.

One possibility is that the octahedral environment of the iron ion in combination with the high-spin state allows a -potentially dynamic- Jahn-Teller effect. We thus have to determine the electronic ground state of the *d*-shell. The Fe^{2+} ion in the trigonally distorted octahedral environment formed by the NCN^{2-} groups, as depicted in Fig. 2.1, has been employed as input for the Effective Hamiltonian Crystal Field (EHCF) method[61,62]. This calculation reveals the ground state of the Fe^{2+} ion to be high-spin, in agreement with previous calculations[49] and the observed isomer shift. The octahedral environment leads to the $^5T_{2g}$ ground state. The trigonal distortion of the octahedral field, induced by the NCN units, further splits this state to the $^5A_1$ state and the spatially degenerate ^5E states. Our calculation by the EHCF method shows that the true ground state is precisely the spatially non-degenerate $^5A_1$ state, in agreement with the negative sign of the quadrupole interaction as also outlined in Ref. (23). In case of a ^5E ground state, the quadrupole interaction would

be positive. The ^5E state is estimated to be 320 K above the ground state. Although this calculation is close to the border of its precision, it may indicate a possible thermal population of the ^5E states. This thermal population is directly seen in the temperature dependence of the quadrupole interaction. An estimation of the temperature-dependent quadrupole interaction according to the Ingalls model[26], with or without lattice contribution, leads to a splitting between the $^5A_1$ and ^5E states ranging between 500 and 900 K. Due to the $^5A_1$ ground state and the absence of any step-like change[63] in isomer shift or quadrupole splitting a (dynamic) Jahn-Teller effect can be ruled out.

Another possibility to consider is a high-to-low spin transition. We found no indication for such a transition[22], because the isomer shift changes smoothly and no step-like change was observed. Also the Mössbauer temperature for the second order Doppler-shift of 451(30) K is reasonable and does not indicate any strong change.

Summarising, a transition within the *d*-orbitals, which would lead to the observed behaviour of the hyperfine field and the angle θ is thus quite unlikely. However, the covalency of the Fe−N bond was not considered so far. Because the electronegativity of N as compared to O is closer to iron, the bond will be more covalent and a stronger super-exchange is expected[64,65]. Thus the covalency could be a reason for the large Néel temperature of FeNCN as compared to FeO but it does not explain the exceptional behaviour of iron within the *M*NCN series, since the bonding character in the series should be the same. A second consequence of the increasing covalency is a reduction of the Fermi contact term[66,67]. This reduction might explain the exceptionally strong reduction in hyperfine field of component I as compared to the iron oxide. The theoretical value of the Fermi contact field would be 11 T per spin[24] leading to 44 T for Fe(II) high spin. The observed hyperfine field of component I is around 2 T at low temperatures and thus indicates a remarkably small reduction parameter[66–68] of $\kappa = \frac{H_{observed}}{H_{theoretical}} = 0.05$.

Consequently, the previously ignored spin dipole and orbital momentum terms need to be considered for the temperature behaviour of the hyperfine field, as they might have a similar magnitude as the Fermi contact term. Both terms can change with temperature and thus may explain the temperature behaviour of the hyperfine field. By assuming similar asymmetries for the charge density and the spin density, the dipolar interaction term can be described as[24,69] $|B_D| = \mu_B V_{zz} e$. The orbital momentum term will be zero at low temperatures due to the nondegeneracy of the $^5A_1$ state, *i.e.*, the orbital quenching. With increasing temperature, the ^5E state will be populated due to thermal excitation. This scenario can be observed in the strong temperature dependence of the quadrupole interaction, which is directly linked to the thermal population of these levels[26]. The sum of the arising orbital momentum term and the dipole term change the hyperfine magnetic field by around 3 T between 10 K and room temperature, assuming that the Fermi contact term stays constant. Above room temperature, the total field drops again due to the vanishing sublattice magnetisation at the Néel temperature.

The interplay between the hyperfine field contributions could also explain the observed change in the angle θ, under the assumption that the low temperature field, likely oriented at 60 degrees from the c-axis, and the temperature-dependent orbital and dipolar terms are not (anti-)parallel. Furthermore, the larger T_N in FeNCN as compared to other metals could also be related to the arising orbital momentum. This mechanism is not possible for all NCN compounds, because Mn^{2+} is a $3d^5$ system and has a singlet ground state, thus no orbital momentum can be formed,

likewise for Ni^{2+} with filled t_{2g} levels. However, for Co^{2+} Jahn-Teller effect or orbital momentum are possible and the transition temperature in CoNCN is also quite high, close to the related oxide.

The suggested model implies a change of the total atomic moment in size and direction with changing temperature. This hypothesis can not be verified directly by magnetometry due to the antiferromagnetic order. Further experiments will have to be performed in order to gain a deeper insight, such as a magnetic structure refinement of neutron diffraction data, absorption spectroscopy, and also high resolution temperature-dependent X-ray diffraction in order to check for any structural distortion that might occur.

2.5 Conclusion

We have presented measurements of FeNCN, featuring similarities and differences to the related iron monoxide. The Mössbauer spectroscopic data exhibit the same Fe^{2+} state for iron with a similar octahedral coordination environment but with a completely different and unconventional temperature behaviour of the hyperfine field, it decreases upon lowering the temperature. Furthermore, a temperature-dependent reorientation of the hyperfine magnetic field from 90° at room temperature to 60° at 6 K was observed, with respect to the *c* axis. Both observed phenomena are likely correlated due to the qualitatively similar behaviour. A study of different possible effects on the *d*-orbitals leads to the conclusion that an interplay between a strongly reduced hyperfine field and a temperature-dependent dipole and orbital momentum contribution to the hyperfine field can explain the observed behaviour.

The extracted DPS from the NIS data of FeNCN has a similar shape as compared to FeO due to the similar local environment and the similar bonding, but exhibits a softening with a low-energy phonon mode between 4 and 8 meV. The obtained Debye level of FeNCN is similar to literature values of FeO, however slightly increased. The magnetometry data reveals the Néel temperature at $\approx$ 350 K and exhibits a splitting of the ZFC/FC curves between Néel temperature and 5 K, this splitting might indicate impurities in the antiferromagnetic order.

Volume 38 | Number 10 | October 2014 | Pages 4633–5098

NJC

New Journal of Chemistry
www.rsc.org/njc

A journal for new directions in chemistry

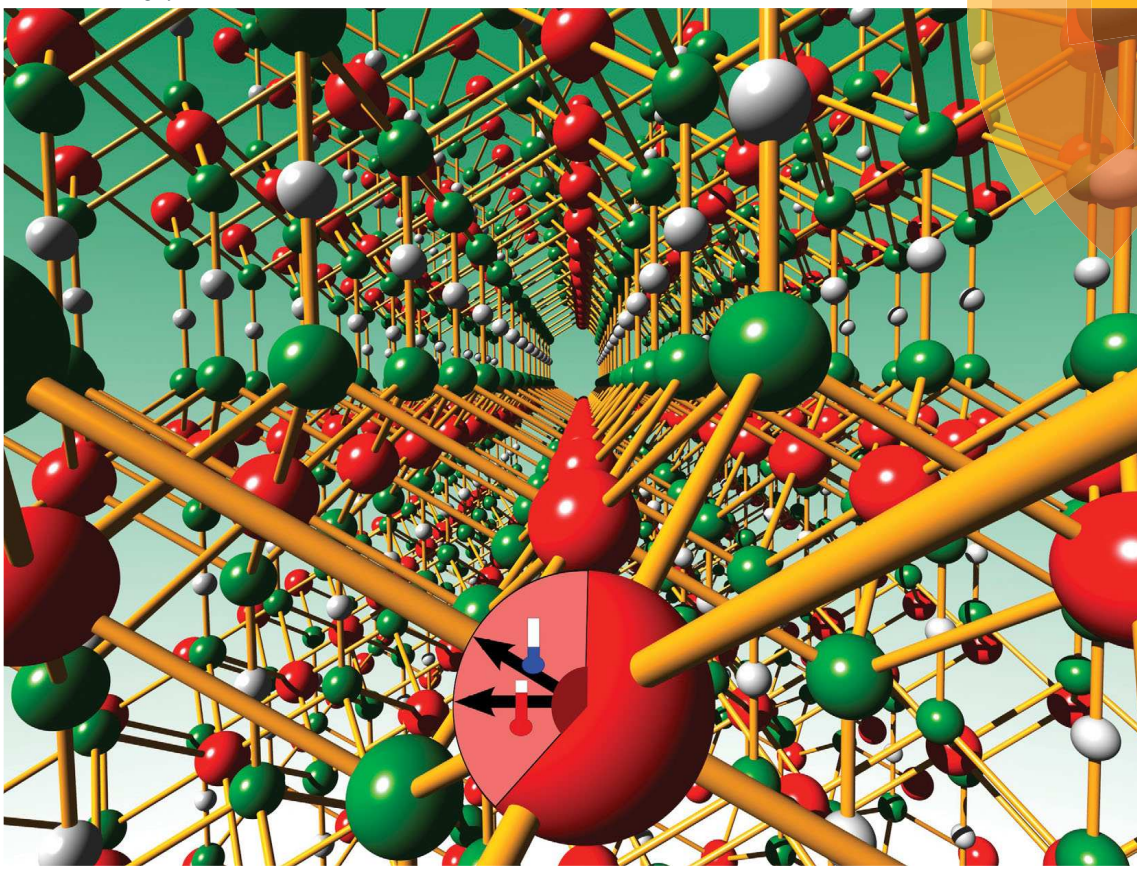

ISSN 1144-0546

ROYAL SOCIETY OF CHEMISTRY

PAPER
M. Herlitschke *et al.*
Magnetism and lattice dynamics of FeNCN compared to FeO

cnrs

Chapter 3

Chapter 6

6 Summary

The results obtained on the recently synthesized FeNCN material reveals a complex behaviour of the hyperfine parameters as a function of temperature. The quadrupole interaction and the hyperfine field are strongly dependent on temperature. In addition, the observed decrease of the hyperfine field with decreasing temperature is very uncommon. The observations are discussed with respect to the temperature dependence of the *d*-orbitals population. A small Fermi contact term and an arising orbital momentum term with increasing temperature cause these effects. Furthermore, the angle between the electric field gradient and the hyperfine field changes with temperature in the magnetically ordered state, which is consistent with the proposed model. The magnetometry data indicates a large amount of defects, impurities or vacancies in the FeNCN structure. This result is in agreement with the Mössbauer spectral data revealing a second phase with an isomer shift common for Fe^{3+}. A deeper analysis of the magnetic order in FeNCN with neutron scattering and in-field Mössbauer spectroscopy is currently ongoing.

The $Mn_{5-x}Fe_xSi_3$ series exhibits several effects upon changing x, *e.g.*, change of the hyperfine field of the 6*g* site on increasing iron content, and different magnetic orders. These effects are not entirely understood but the reported investigations are discussed with comparison to literature. The presented studies reveal that the magnetocaloric effect in $MnFe_4Si_3$ only weakly influences the high energy phonons, whereby the vibrational entropy of the system can only change by about 1 %. In contrast, the elasticity, associated to low energy phonon modes, is strongly influenced by the magnetocaloric transition, as determined with RUS. A soft mode behaviour in the elasticity mainly appears in the $a - b$ plane of the hexagonal system, thus this region is of high interest in understanding the mechanism of the magnetocaloric effect in this material. In order to clarify the spin structure in this material and foster the understanding of the dynamic behaviour, elastic and inelastic neutron experiments are planned as objectives for another PhD thesis in the JCNS-2 institute.

The maghemite nanospheres are characterized with Mössbauer spectroscopy, magnetometry and small-angle X-ray scattering (SAXS). The latter measurement was performed *in-situ* on the samples subsequently used for nuclear forward scattering (NFS) in order to observe any possible agglomeration of the particles. The investigation of the maghemite nanospheres with NFS revealed the spin orientation in this material in dependence of the applied magnetic field. A model is proposed, which describes the spin orientation with one or two scalar variables, depending on the field direction. Less than 60 % of the spins orient parallel to magnetic field of up to 7.5 T, whereas the majority of these spins align already in fields of less than half a Tesla. The modeled magnetization, calculated from this relative spin orientation, matches excellently the macroscopic measurements and literature values. Similar results were obtained with in-field Mössbauer spectroscopy, analysed

with a model similar to the NFS model. Possible expansions of the presented investigation are, for example, measurements in high magnetic fields oriented along the beam direction, and the application of polarization analysis. Both improvements give access to further information on the spin orientation by yielding the polarization switching term, G_m, of the NFS amplitudes.

The application of the ^{57}Fe nuclear resonance to the small-angle scattering technique revealed no additional information on the maghemite nanospheres, as compared to usual SAXS. This fact is most probably reasoned by a large non-resonant scattering cross section for this material. However, the nanostructered alloy, which exhibits a smaller difference in the scattering length density of the nanoparticles and their surrounding, has an obvious contribution from the nuclear resonant small-angle scattering process. The results allow one to determine the particle size, which is in agreement with literature values. Furthermore, it seems that the non-resonant scattering has additional contribution from particles without iron content and thus the applied resonant technique allows one to highlight the scattering from the embedded bcc-iron particles. Possible further investigations are, for example, partial enrichment in order to highlight certain regions in a material, use of polarization analysis, and recording of time spectra at small scattering angles. These improvements can give additional information on the hyperfine field distribution in nanomaterials.

Bibliography

[1] L. D. Landau and E. M. Lifshitz, *Theory of Elasticity*, Butterworth Heinemann, 3rd edn, 2002, vol. 7.

[2] C. Kittel, *Introduction to Solid State Physics*, John Wiley, 7th edn, 1996.

[3] A. Migliori and J. Sarrao, *Resonant Ultrasound Spectroscopy: Applications to Physics, Materials Measurements, and Nondestructive Evaluation*, John Wiley & Sons Inc, 1997.

[4] R. Hill, *Proceedings of the Physical Society. Section A*, 1952, **65**, 349.

[5] X. Tao, P. Jund, C. Colinet and J. Tedenac, *Phys. Rev. B*, 2009, **80**, 104103.

[6] R. Gross and A. Marx, *Festkörperphysik*, Oldenburg Verlag, 2012.

[7] R. Rüffer and A. Chumakov, *Hyperfine Interactions*, 2000, **128**, 255–272.

[8] A. Chumakov and R. Rüffer, *Hyperfine Interactions*, 1998, **113**, 59–79.

[9] M. Hu, W. Sturhahn, T. Toellner, P. Mannheim, D. Brown, J. Zhao and E. Alp, *Phys. Rev. B*, 2003, **67**, 094304.

[10] M. T. Dove, *Introduction to Lattice Dynamics*, Cambridge University Press, 1993.

[11] S. Blundell, *Magnetism in Condensed Matter*, Oxford, 2001.

[12] J. M. D. Coey, *Magnetism and Magnetic Materials*, Cambridge, 2010.

[13] P. Mohn, *Magnetism in the Solid State*, Springer, 2006.

[14] S. Disch, R. P. Hermann, E. Wetterskog, A. A. Podlesnyak, K. An, T. Hyeon, G. Salazar-Alvarez, L. Bergström and T. Brückel, *Phys. Rev. B*, 2014, **89**, 064402.

[15] G. F. Goya, T. S. Berquo, F. C. Fonseca and M. P. Morales, *Journal of Applied Physics*, 2003, **94**, 3520–3528.

[16] O. Tegusi, *PhD thesis*, Universiteit van Amsterdam, 2003.

[17] S. Fishman and A. Aharony, *Journal of Physics C: Solid State Physics*, 1979, **12**, L729.

[18] T. Nattermann, *Spin Glasses And Random Fields: Series on Directions in Condensed Matter Physics*, 1997, **12**, 277.

[19] F. Monenegro, S. Rezende and M. Coutinho-Filho, *RBrFi*, 1991, **21**, 192.

[20] B. Povh, K. Rith, C. Scholz, F. Zetsche and M. Lavelle, *Particles and Nuclei*, Springer, 2008.

[21] G. Schatz and A. Weidinger, *Nuclear Condensed Matter Physics*, Wiley, 1995.

[22] P. Gütlich, E. Bill and A. X. Trautwein, *Mössbauer Spectroscopy and Transition Metal Chemistry*, Springer, 2011.

[23] G. J. Long, *Mössbauer Spectroscopy Applied to Inorganic Chemistry*, Plenum Press, 1984.

[24] N. N. Greenwood and T. C. Gibb, *Mössbauer Spectroscopy*, Chapman and Hall Ltd, 1971.

[25] R. Sternheimer, *Phys. Rev.*, 1952, **86**, 316–324.

[26] R. Ingalls, *Phys. Rev.*, 1964, **133**, A787–A795.

[27] M. Angst, T. Brückel, D. Richter and R. Zorn, *Scattering Methods for Condensed Matter Research*, Schriften des Forschungszentrums Jülich, 2012.

[28] D. I. Feigin, L. A.and Svergun, *Structure Analysis by Small-Angle X-Ray and Neutron Scattering*, Plenum Press, 1987.

[29] N. Ashcroft and D. Mermin, *Solid State Physics*, Cornell University, 1976.

[30] C. Voyer and D. Ryan, *Hyperfine Interact*, 2006, **170**, 91–104.

[31] G. J. Long, *MERDJ*, 1983, **6**, 42.

[32] J. M. Greneche and F. Varret, *Journal of Physics C: Solid State Physics*, 1982, **15**, 5333.

[33] U. Gonser, F. Aubertin, S. Stenger, H. Fischer, G. Smirnov and G. Klingelhöfer, *Hyperfine Interactions*, 1991, **67**, 701–709.

[34] R. Röhlsberger, *Nuclear Condensed Matter Physics with Synchrotron Radiation*, Springer, 2004.

[35] S. Dattagupta, *Hyperfine Interact*, 1981, **11**, 77–126.

[36] Y. V. Shvyd'ko, *Hyperfine Interact*, 1999, **123-124**, 275–299.

[37] H. Weiss and H. Langhoff, *Physics Letters A*, 1979, **69**, 448–450.

[38] V. Kohn and A. Chumakov, *Hyperfine Interact.*, 2000, **125**, 205.

[39] K. Terakura, T. Oguchi, A. R. Williams and J. Kübler, *Phys. Rev. B*, 1984, **30**, 4734.

[40] B. Koiller and L. M. Falicov, *Journal of Physics C: Solid State Physics*, 1975, **8**, 695.

[41] X. Liu, M. Krott, P. Müller, C. Hu, H. Lueken and R. Dronskowski, *Inorg. Chem.*, 2005, **44**, 3001.

[42] C. Janiak, *Dalton Trans.*, 2003, 2781.

[43] O. Kahn, J. Larionova and L. Ouahab, *Chem. Commun.*, 1999, 945.

[44] M. Krott, X. Liu, B. P. T. Fokwa, M. Speldrich, H. Lueken and R. Dronskowski, *Inorg. Chem.*, 2007, **46**, 2204.

[45] X. Liu, R. Dronskowski, R. K. Kremer, M. Ahrens, C. Lee and M.-H. Whangbo, *J. Phys. Chem. C*, 2008, **112**, 11013.

[46] X. Liu, L. Stork, M. Speldrich, H. Lueken and R. Dronskowski, *Chem. Eur. J.*, 2009, **15**, 1558.

[47] A. Tsirlin, K. Koepernik and H. Rosner, *ArXiv e-prints*, 2011, 1106.3665.

[48] H. Xiang, R. Dronskowski, B. Eck and A. L. Tchougréeff, *J. Phys. Chem. A*, 2010, **114**, 12345–12352.

[49] A. L. Tchougréeff and R. Dronskowski, *J. Phys. Chem. A*, 2011, **115**, 4547–4552.

[50] H. Fjellvaag, F. Gronvold, S. Stolen and B. Hauback, *Journal of Solid State Chemistry*, 1996, **124**, 52.

[51] G. Srinivasan and M. Seehra, *Phys. Rev. B*, 1983, **28**, 6542.

[52] G. Kugel, C. Carabatos, B. Hennion, B. Prevot, A. Revcolevschi and D. Tocchetti, *Phys. Rev. B*, 1977, **16**, 378.

[53] M. Blume, *Phys. Rev.*, 1968, **174**, 351.

[54] S. Dattagupta and M. Blume, *Phys. Rev. B*, 1974, **10**, 4540.

[55] W. Sturhahn, T. Toellner, E. Alp, X. Zhang, M. Ando, Y. Yoda, S. Kikuta, M. Seto, C. Kimball and B. Dabrowski, *Phys. Rev. Lett.*, 1995, **74**, 3832–3835.

[56] N. Greenwood and A. Howe, *J. Chem. Soc., Dalton Trans.*, 1972, 110.

[57] J. A. Mydosh, *Spin Glass*, Taylor &Francis, 1993.

[58] M. J. Benitez, O. Petracic, E. L. Salabas, F. Radu, H. Tüysüz, F. Schüth and H. Zabel, *Phys. Rev. Lett.*, 2008, **101**, 097206.

[59] M. Inazumi, Y. Nakagawa, M. Tanaka, N. Kimizuka and K. Siratori, *J. Phys. Soc. Jpn.*, 1981, **50**, 438.

[60] V. Struzhkin, H. Mao, J. Hu, M. Schwoerer-Böhning, J. Shu and R. Hemley, *Phys Rev Lett*, 2001, **87(25)**, 255501.

[61] A. Soudackov, A. Tchougréeff and I. Misurkin, *Theor. Chim. Acta*, 1992, **83**, 389–416.

[62] A. Soudackov and K. Jug, *Int. J. Quant. Chem.*, 1996, **62**, 403.

[63] M. Tanaka, T. Tokoro and Y. Aiyama, *J. Phys. Soc. Jpn.*, 1966, **21**, 262–267.

[64] T. R. Waite, *The Journal of Chemical Physics*, 1960, **33**, 256–265.

[65] J. B. Goodenough and A. L. Loeb, *Phys. Rev.*, 1955, **98**, 391–408.

[66] J. Henning, *Physics Letters A*, 1967, **24**, 40–42.

[67] W. T. Oosterhuis and G. Lang, *Phys. Rev.*, 1969, **178**, 439–456.

[68] H. Andres, E. L. Bominaar, J. M. Smith, N. A. Eckert, P. L. Holland and E. Münck, *J. Am. Chem. Soc.*, 2002, **124**, 3012–3025.

[69] F. van der Woude, *phys. stat. sol. (b)*, 1966, **17**, 417–432.

[70] E. Brück, *Journal of Physics D: Applied Physics*, 2005, **38**, R381.

[71] K. A. Gschneidner Jr, V. K. . Pecharsky and A. O. Tsokol, *Reports on Progress in Physics*, 2005, **68**, 1479.

[72] E. Warburg, *Ann. Phys.*, 1881, **249**, 141–164.

[73] W. F. Giauque and D. P. MacDougall, *Phys. Rev.*, 1933, **43**, 768–768.

[74] N. A. de Oliveira and P. J. von Ranke, *Physics Reports*, 2010, **489**, 89–159.

[75] V. K. Pecharsky and K. A. Gschneidner, *Journal of Applied Physics*, 1999, **86**, 565–575.

[76] P. Hering, *MSc thesis*, RWTH Aachen, FZ Jülich, 2014.

[77] L. Song, W. Dagula, O. Tegus, E. Brück, J. Klaasse, F. de Boer and K. Buschow, *Journal of Alloys and Compounds*, 2002, **334**, 249–252.

[78] V. Franco, J. Blázquez, B. Ingale and A. Conde, *Annual Review of Materials Research*, 2012, **42**, 305–342.

[79] H. Bińczycka, v. Dimitrijević, B. Gajić and A. Szytula, *physica status solidi (a)*, 1973, **19**, K13–K17.

[80] V. Johnson, J. Weiher, C. Frederick and D. Rogers, *Journal of Solid State Chemistry*, 1972, **4**, 311–323.

[81] A. Migliori, J. Sarrao, W. M. Visscher, T. Bell, M. Lei, Z. Fisk and R. Leisure, *Physica B*, 1993, **183**, 1–24.

[82] T. Moriya and Y. Takahashi, *Annual Review of Materials Science*, 1984, **14**, 1–25.

[83] R. Haug, G. Kappel and A. Jaegle, *Journal of Physics and Chemistry of Solids*, 1980, **41**, 539–544.

[84] A. Candini, O. Moze, W. Kockelmann, J. M. Cadogan, E. Brück and O. Tegus, *Journal of Applied Physics*, 2004, **95**, 6819–6821.

[85] P. A. Grünberg, *Rev. Mod. Phys.*, 2008, **80**, 1531–1540.

[86] R. P. Hermann, O. Tegus, E. Brück, K. H. J. Buschow, F. R. de Boer, G. J. Long and F. Grandjean, *Phys. Rev. B*, 2004, **70**, 214425.

[87] M. T. Sougrati, R. P. Hermann, F. Grandjean, G. J. Long, E. Brück, O. Tegus, N. T. Trung and K. H. J. Buschow, *Journal of Physics: Condensed Matter*, 2008, **20**, 475206.

[88] D. Bessas, W. Tollner, Z. Aabdin, N. Peranio, I. Sergueev, H. Wille, O. Eibl, K. Nielsch and R. P. Hermann, *Nanoscale*, 2013, **5**, 10629–10635.

[89] K. Narasimhan, W. Reiff, H. Steinfink and R. Collins, *Journal of Physics and Chemistry of Solids*, 1970, **31**, 1511–1524.

[90] C. P. Bean and D. S. Rodbell, *Phys. Rev.*, 1962, **126**, 104–115.

[91] W. Rehwald, *Advances in Physics*, 1973, **22**, 721–755.

[92] D. Bessas, K. Z. Rushchanskii, M. Kachlik, S. Disch, O. Gourdon, J. Bednarcik, K. Maca, I. Sergueev, S. Kamba, M. Lezaić and R. P. Hermann, *Phys. Rev. B*, 2013, **88**, 144308.

[93] P. Bauer-Pereira, *PhD thesis*, University of Liège (Belgium), 2012.

[94] W. Wettling, W. Jantz and H. Dötsch, *Applied physics*, 1980, **23**, 195–198.

[95] N. W. Ashcroft and N. D. Mermin, *Solid State Physics*, WILEY-VCH Verlag, 1978, vol. 9, pp. 33–33.

[96] S. D. Bader, *Rev. Mod. Phys.*, 2006, **78**, 1–15.

[97] B. Kozissnik and J. Dobson, *MRS Bulletin*, 2013, **38**, 927–932.

[98] Q. A. Pankhurst, J. Connolly, S. K. Jones and J. Dobson, *Journal of Physics D: Applied Physics*, 2003, **36**, R167.

[99] K. J. M. Bishop, C. E. Wilmer, S. Soh and B. A. Grzybowski, *Small*, 2009, **5**, 1600–1630.

[100] S. Disch, E. Wetterskog, R. P. Hermann, G. Salazar-Alvarez, P. Busch, T. Brückel, L. Bergström and S. Kamali, *Nano Lett.*, 2011, **11**, 1651–1656.

[101] J. B. Tracy and T. M. Crawford, *MRS Bulletin*, 2013, **38**, 915–920.

[102] S. G. Morrish, A.H., *Proc. Int. Conf. Ferrites, University of Tokyo Press*, 1971, 144.

[103] H. Batis-Landoulsi and P. Vergnon, *J Mater Sci*, 1983, **18**, 3399.

[104] J. M. D. Coey, *Phys. Rev. Lett.*, 1971, **27**, 1140–1142.

[105] E. Tronc, P. Prené, J. Jolivet, J. Dormann and J. Grenèche, *Hyperfine Interact*, 1998, **112**, 97–100.

[106] S. Mørup, *Journal of Magnetism and Magnetic Materials*, 2003, **266**, 110–118.

[107] S. Disch, E. Wetterskog, R. P. Hermann, A. Wiedenmann, U. Vainio, G. Salazar-Alvarez, L. Bergström and T. Bückel, *New Journal of Physics*, 2012, **14**, 013025.

[108] R. Kodama, *Journal of Magnetism and Magnetic Materials*, 1999, **200**, 359–372.

[109] M. P. Morales, S. Veintemillas-Verdaguer, M. I. Montero, C. J. Serna, A. Roig, L. Casas, B. Martinez and F. Sandiumenge, *Chem. Mater.*, 1999, **11**, 3058–3064.

[110] J. Restrepo, Y. Labaye and J. Greneche, *Physica B: Condensed Matter*, 2006, **384**, 221–223.

[111] K. L. Krycka, R. A. Booth, C. R. Hogg, Y. Ijiri, J. A. Borchers, W. C. Chen, S. M. Watson, M. Laver, T. R. Gentile, L. R. Dedon, S. Harris, J. J. Rhyne and S. A. Majetich, *Phys. Rev. Lett.*, 2010, **104**, 207203.

[112] E. Tronc, R. Ezzir, A .and Cherkaoui, C. Chanéac, M. Noguès, H. Kachkachi, D. Fiorani, A. M. Testa, J. M. Grenèche and J. P. Jolivet, *Journal of Magnetism and Magnetic Materials*, 2000, **221**, 63–79.

[113] J.-E. Jorgensen, L. Mosegaard, L. E. Thomsen, T. R. Jensen and J. C. Hanson, *Journal of Solid State Chemistry*, 2007, **180**, 180–185.

[114] J. G. Long, *Mössbauer Spectroscopy Applied to Inorganic Chemistry Volume 2*, Plenum Press, 1987.

[115] J. Park, K. An, Y. Hwang, J.-G. Park, H.-J. Noh, J.-Y. Kim, J.-H. Park, N.-M. Hwang and T. Hyeon, *Nat Mater*, 2004, **3**, 891.

[116] G. Salazar-Alvarez, J. Qin, V. Sepelák, I. Bergmann, M. Vasilakaki, K. N. Trohidou, J. D. Ardisson, W. A. A. Macedo, M. Mikhaylova, M. Muhammed, M. D. Baró and J. Nogués, *J. Am. Chem. Soc.*, 2008, **130**, 13234.

[117] E. Wetterskog, C.-W. Tai, J. Grins, L. Bergström and G. Salazar-Alvarez, *ACS Nano*, 2013, **7**, 7132–7144.

[118] S. Bedanta, O. Petracic and W. Kleemann, *Handbook Of Magnetism Vol. 22*, in print, 2014.

[119] F. Wiekhorst, E. Shevchenko, H. Weller and J. Kötzler, *Phys. Rev. B*, 2003, **67**, 224416.

[120] P. Dutta, A. Manivannan, M. S. Seehra, N. Shah and G. P. Huffman, *Phys. Rev. B*, 2004, **70**, 174428.

[121] J. B. Tracy, D. N. Weiss, D. P. Dinega and M. G. Bawendi, *Phys. Rev. B*, 2005, **72**, 064404.

[122] J. Nogués and I. K. Schuller, *Journal of Magnetism and Magnetic Materials*, 1999, **192**, 203–232.

[123] Y. V. Shvyd'ko, *Hyperfine Interactions*, 2000, **125**, 173–188.

[124] C. Strohm, P. Van der Linden and R. Rüffer, *Phys. Rev. Lett.*, 2010, **104**, 087601.

[125] M. P. Morales, C. J. Serna, F. Bodker and S. Mørup, *Journal of Physics: Condensed Matter*, 1997, **9**, 5461.

[126] L. Häggström, S. Kamali, T. Ericsson, P. Nordblad, A. Ahniyaz and L. Bergström, *ICAME 2007*, Springer Berlin Heidelberg, 2009, pp. 221–225.

[127] O. Helgason, H. K. Rasmussen and S. Morup, *Journal of Magnetism and Magnetic Materials*, 2006, **302**, 413–420.

[128] S. Mørup, E. Brok and C. Frandsen, *Journal of Nanomaterials*, 2013, **2013**, 8.

[129] R. H. Kodama, A. E. Berkowitz, E. J. McNiff, Jr. and S. Foner, *Phys. Rev. Lett.*, 1996, **77**, 394–397.

[130] J. G. Stevens, A. M. Khasanov, N. F. Hall and K. I. A., *Mössbauer Spectroscopy Newsletter - 50 years of the Mössbauer effect*, online download, 2008, `http://www.medc.dicp.ac.cn/Newsletter.php`.

[131] W. Kündig, H. Bömmel, G. Constabaris and R. H. Lindquist, *Phys. Rev.*, 1966, **142**, 327–333.

[132] Q. Pankhurst, *Hyperfine Interactions*, 1994, **90**, 201–214.

[133] J. B. Hastings, D. P. Siddons, U. van Bürck, R. Hollatz and U. Bergmann, *Phys. Rev. Lett.*, 1991, **66**, 770–773.

[134] P. Lindner and T. Zemb, *Neutron, X-rays and Light: Scattering Methods Applied to Soft Condensed Matter*, North-Holland, 2002.

[135] Y. V. Shvyd'ko, A. I. Chumakov, A. Q. R. Baron, E. Gerdau, R. Rüfer, A. Bernhard and J. Metge, *Phys. Rev. B*, 1996, **54**, 14942–14945.

[136] D. L. Nagy, L. Bottyan, B. Croonenborghs, L. Deak, B. Degroote, J. Dekoster, H. J. Lauter, V. Lauter-Pasyuk, O. Leupold, M. Major, J. Meersschaut, O. Nikonov, A. Petrenko, R. Rüffer, H. Spiering and E. Szilágyi, *Phys. Rev. Lett.*, 2002, **88**, 157202.

[137] A. Ahniyaz, Y. Sakamoto and L. Bergström, *Proceedings of the National Academy of Sciences*, 2007, **104**, 17570–17574.

[138] M. Miglierini and J.-M. Greneche, *Journal of Physics: Condensed Matter*, 1997, **9**, 2303.

[139] B. Idzikowski, P. Svec and M. M., *Properties and Applications of Nanocrystalline Alloys from Amorphous Precursors*, Springer Netherlands, 2005.

[140] M. Miglierini, M. Kopcewicz, B. Idzikowski, Z. E. Horvath, A. Grabias, I. Skorvanek, P. Duzewski and C. S. Daroczi, *Journal of Applied Physics*, 1999, **85**, 1014–1025.

[141] M. Miglierini, T. Kanuch, M. Pavuk, Y. Jiraskova, R. Zboril, M. Maslan and P. Svec, *The Physics of Metals and Metallography*, 2007, **104**, 335–345.

[142] E. Illekova, D. Janickovic, M. Miglierini, I. Skorvanek and P. Svec, *Journal of Magnetism and Magnetic Materials*, 2006, **304**, e636–e638.

[143] M. Miglierini, *Journal of Non-Crystalline Solids*, 2008, **354**, 5093–5096.

[144] M. Paluga, P. Svec, D. Janickovic, D. Muller, P. Mrafko and M. Miglierini, *Rev. Adv. Mater. Sci.*, 2008, **18**, 481–493.

[145] S. Hansen, *Journal of Applied Crystallography*, 2014, **47**, 1469–1471.

[146] R. Röhlsberger, *Hyperfine Interactions*, 1999, **123-124**, 301–325.